A CONTINUUM-MOLECULAR MODEL FOR ANISOTROPIC ELECTRICALLY CONDUCTIVE MATERIALS

Vito Diana[a,*], Valter Carvelli[b]

[a] *Department of Civil, Chemical and Environmental Engineering, University of Genova, via Montallegro 1, 16145 Genova, Italy*

[b] *Department ABC, Politecnico di Milano, Piazza Leonardo da Vinci 32, Milano, 20133 Italy*

Abstract

An anisotropic model for two-dimensional electrical conduction, elasticity and fracture is proposed in the peridynamic theoretical framework. Material particles interact through elastic non-central pair potentials and inelastic pair potential functions of pairwise elastic and inelastic deformation measure, allowing to obtain a bond-based type model for conductive Cauchy orthotropic media without restrictions in the number of independent material constants. The elasticity of pair interactions can be described mechanistically by equivalent normal and shear springs, whose stiffness varies continuously with the spatial orientation of the ligament and, preserving the elastic symmetries of the material, depends on four elastic material parameters defining in-plane orthotropic classical elasticity. The macroscopic anisotropic conductivity is described instead by continuous functions of the micro-conductive properties of the interparticles interactions. Moreover, non-uniform material toughness is modeled adopting an anisotropic energetic failure criterion related to direction-dependent fracture energy functionals.
The accuracy of the proposed model has been assessed by several problems including the anisotropic electrical conduction in multi-phases laminae with a central hole and evolving cracks, and the fracture and damage sensing in cortical bone considering different orientation of the material reference system.

Keywords: Anistropy, Peridynamics, Conductivity, Fracture, Damage sensing

1. Introduction

Mechanistic models in applied sciences based on the concept of action at a distance have shown to provide an effective and intuitive description of a wide variety of physical phenomena spacing from elasticity, fracture, diffusion and coupled behaviors [1, 2, 3]. Suitability to fracture problems of these molecular theory of elasticity [4, 5] inspired models was clearly demonstrated, among others, by Silling [6] who proposed a mechanical non-local displacement-based formulation, namely Peridynamics, in which the governing equations remain valid in the presence of discontinuities such as cracks [1, 7]. Silling's theory is non-local, which means that material points interact within a cut-off distance, the horizon, that can be considered a generalization of the concept of ray of molecular activity characterizing Cauchy and Navier molecular models [8]. As for the latter, in the original proposed theory, referred to as bond-based, forces depend on the distance between pairs of molecules and act long the line joining the points, hence, as in Navier's theory [8, 9], Cauchy relations hold [10]. A non-local continuum formulation results useful in a computational context, as it allows, in principle, for decoupling the analytical

*Corresponding author, e-mail: vito.diana@unige.it

mathematics of the model from the lattice topology of the discretized medium. This aspect is particularly important for direction-dependent material properties, and in fracture problems since it drastically reduces intrinsic mesh dependency of the results and failure anisotropy typical of lattice models [5]. To overcome restrictions imposed by Cauchy relations, more general formulations were introduced [11], named state-based and non-ordinary state-based [12], in which the pairwise force between two particles depends on the deformations of all nodes within their neighborhood. Hence, material points still interact through forces acting at a distance, requiring however the definition of point-wise deformation measures, namely the deformation states [13]. A first attempt to overcome the aforementioned limitations maintaining a pairwise formalism, is due to Gerstle et al. [14] augmenting degrees of freedom in classical peridynamics. The general formulation used to describe mechanical problems allows the concept of action at a distance to be generalized and extended to other physical fields involving diffusion [15], electromigration [16], electrical conduction [17, 18], heat transfer [19, 20] and pitting corrosion [21]. Other applications of peridynamics for thermo-mechanics or other multi-physics problems can be found in [22, 23, 15, 24].

In any case, much attention has been paid to isotropic materials, whose stiffness, conductivity and strength properties are not direction-dependent, while relatively few studies of anisotropic materials have been carried out [25, 26, 27]. In the context of anisotropic elasticity, continuum peridynamic formulations without internal constrains affecting the material moduli, were possible only by disregarding the paradigm of purely pairwise interactions [28, 26], being the other continuum bond-based type models affected by restrictions in the number of independent material constants [27, 29, 30]. Recently, a continuum-kinematic inspired peridynamic model for orthotropic materials has been presented [31], which is characterized by three over four independent moduli defining Cauchy in-plane orthotropic elasticity. For the best of authors' knowledge, a continuum model with pairwise interactions (functions of pairwise deformations and constitutive parameters) for orthotropic elasticity, conductivity and fracture in Cauchy materials without limitation in the number of independent material constants, along with a general framework for deriving the related model parameters, have not been proposed so far.

Actually, a purely pairwise formalism provides an easier understanding and a very intuitive description of several physical phenomena, since each pair interaction can be described mechanistically as an independent multi-physical device. In this paper, we propose an anisotropic non-local continuum model using a purely pairwise description of deformation, elastic parameters, strength and conductivity properties. The elastic part of the model is inspired by Voigt's studies on crystals in the context of molecular theory of elasticity [32], and is capable to overcome Cauchy relations for orthotropic materials without introducing any multi-body potential or point-wise deformation measure. Following Voigt's idea, we defined potential functions of elastic and inelastic pairwise deformation measures, from which interactions exerted between pairs of particles can be derived, leading to a mixed mechanistic/energetic mathematical formulation. Anisotropic conductivity and non-uniform strength properties, related to a direction-dependent fracture energy function, are described analytically by continuous functions of the ligament orientation angle. Therefore, the mathematical formulation is, in principle, independent of the discretization and particles topology, whereas the material parameters are derived using a rigorous generalized approach based on energetic equivalence, without the need of any particular assumption on the deformation and electric fields. It should be noted that the mathematical formulation here presented extends the findings of previous studies [33, 34] and introduces a general framework for modeling anisotropic response of materials. The mechanical model couples the intuitive simplicity of the pairwise description of deformation, with the mathematical formalism of a continuum formulation for anisotropic materials. The proposed formulation can also be adapted to other diffusion problems and coupled behaviors in Cauchy

materials or to the context of micropolar elasticity [35].
The analytical formulations of orthotropic conduction and elasticity of Cauchy materials are detailed in Sections 2 and 3, as well as the analytical description of the mechanical and electrical material model constants. In Section 3.1, an energetic failure criterion for anisotropic brittle conductive materials is proposed. It relates ligament strength to direction-dependent fracture energy functions. The accuracy of the proposed model is illustrated in Section 4 simulating: the effective anisotropic electrical conductive behavior of laminae with homogenized anisotropic properties; the variation of electric resistance in specimens due to an evolving central crack (Section 4.1); the fracture propagation and damage sensing in cortical bone compact tensile test specimens considering different orientation of the material reference system (Section 4.2).

2. The electrical conduction model

The field equation of the electrical conduction for a continuum whose material points $\mathbf{x}$ within a finite distance δ interact through pairwise potentials, e.g. peridynamic continuum, is [34, 18]

$$\int_{H_{\mathbf{x}}} f_I(\mathbf{x}, \mathbf{x}', \phi, \phi') dV_{\mathbf{x}'} + \omega(\mathbf{x}, t) = c_e \dot{\phi}(\mathbf{x}, t) \quad \text{for} \quad \mathbf{x} \in \Omega, \tag{1}$$

where Ω is the domain occupied by the continuum body and the variable t identifies the time. The integral is defined over a region $H_{\mathbf{x}}$ called horizon region of radius δ or family of $\mathbf{x}$ [6]. $\phi = \phi(\mathbf{x})$ and $\phi' = \phi(\mathbf{x}')$ are the electric field potentials at $\mathbf{x}$ and $\mathbf{x}'$, c_e is the electrical capacitance of the material, ω is the net current per unit volume at $\mathbf{x}$. The kernel or integrand function f_I has the dimensions of an electric current per unit volume squared [19, 18].
The steady-state equations are obtained setting the right term of Eq. 1 equal to zero (the time dependent accumulation of electric charge is neglected).
The proposed electrical conduction model is based on the definition of a pairwise parameter $e = -\frac{(\phi' - \phi)}{|\boldsymbol{\xi}|}$ where $\mathbf{x}' - \mathbf{x} = \boldsymbol{\xi}$ is the relative position between the material points $\mathbf{x}$ and $\mathbf{x}'$, that can be considered as the equivalent of a pairwise deformation measure in elasticity, and is function of the ligament electric field defined by

$$\boldsymbol{e} = -\frac{(\phi' - \phi)}{|\boldsymbol{\xi}|} \frac{\boldsymbol{\xi}}{|\boldsymbol{\xi}|} \tag{2}$$

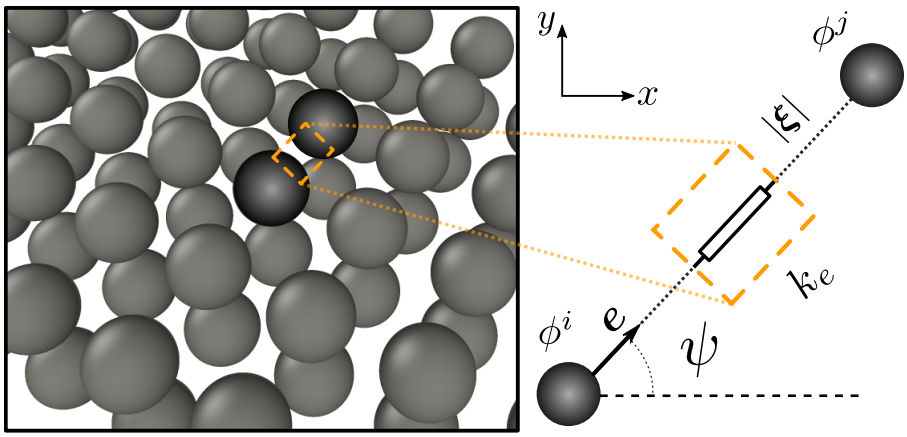

Figure 1: Schematics of the horizon region of particle i, and conductive bond configuration connecting particles i and j in the local/global coordinate system for the proposed electrical conduction model.

It is worth underlying that for the general case of electro-mechanical problems, the bond electric field is directed along the line connecting the two particles in the deformed configuration. However when using linearized electro-mechanical formulations, Eq. 2 holds [34]. The pairwise constitutive equation characterizing the electrical model is derived from the definition of a specific pair inelastic potential function for electrical conduction

$$\mathrm{w}_e = \frac{k_e e^2}{2} = \frac{k_e(\phi' - \phi)^2}{2|\boldsymbol{\xi}|^2} \tag{3}$$

where k_e is the ligament conductivity parameter, namely microconductivity of the electrical model [1], having the dimension of an electric conductivity per unit volume.
The electrical pairwise interaction (namely electrical response function) is then obtained as the first derivative of the potential function w_e

$$f_I = \frac{\partial \mathrm{w_e}}{\partial \eta_\phi} = \frac{k_e\, e}{|\boldsymbol{\xi}|} = \frac{k_e(\phi' - \phi)}{|\boldsymbol{\xi}|^2} \tag{4}$$

where $\eta_\phi = (\phi' - \phi)$. The bond micro-current density vector can be then defined as

$$\boldsymbol{q_I} = k_e\, \boldsymbol{e} \tag{5}$$

The analytical expression of the stiffness operator of the implicit model for electrical conduction can be derived by defining the electrical energy density, namely macroelectrical energy density as

$$\Phi_e(\mathbf{x}) = \frac{1}{2}\int\limits_t \int\limits_{H_\mathbf{x}} \mathrm{w}_e \,\mathrm{dV}_{\mathbf{x}'}\,\mathrm{d}t = \frac{1}{2}\int\limits_t \int\limits_{H_\mathbf{x}} \frac{k_e e^2}{2}\,\mathrm{dV}_{\mathbf{x}'}\,\mathrm{d}t = \frac{1}{2}\int\limits_t \int\limits_{H_\mathbf{x}} \frac{k_e(\phi' - \phi)^2}{2|\boldsymbol{\xi}|^2}\,\mathrm{dV}_{\mathbf{x}'}\,\mathrm{d}t \tag{6}$$

where w_e is defined in Eq. 3, thus the expression of the macroelectric power density

$$P_e(\mathbf{x}) = \frac{1}{2}\int\limits_{H_\mathbf{X}} \mathrm{w}_e \,\mathrm{dV}_{\mathbf{x}'} = \frac{1}{2}\int\limits_{H_\mathbf{x}} \frac{k_e e^2}{2}\,\mathrm{dV}_{\mathbf{x}'} \tag{7}$$

Considering that the total macroelectrical energy functional of the body is

$$\hat{\Phi}_e = \int\limits_\Omega \int\limits_t \int\limits_{H_\mathbf{x}} \frac{k_e e^2}{2}\,\mathrm{dV}_{\mathbf{x}'}\,\mathrm{d}t\,\mathrm{dV}_\mathbf{x} = \int\limits_\Omega \int\limits_t \int\limits_{H_\mathbf{x}} \frac{k_e(\phi' - \phi)^2}{2|\boldsymbol{\xi}|^2}\,\mathrm{dV}_{\mathbf{x}'}\,\mathrm{d}t\,\mathrm{dV}_\mathbf{x} \tag{8}$$

and that the work $\mathcal{L}$ associated with the external actions (the net current) per unit volume ω can be expressed as

$$\mathcal{L} = \frac{1}{2}\int\limits_\Omega \int\limits_t \omega\phi\,\mathrm{d}t\,\mathrm{dV}_\mathbf{x} \tag{9}$$

the equivalence of the internal and external works of the balanced system $(q_I = k_e e, \omega)$ and the compatible system (e, ϕ) is

$$\hat{\Phi}_e = \mathcal{L} \rightarrow \int\limits_\Omega \int\limits_t \int\limits_{H_\mathbf{x}} \frac{k_e(\phi' - \phi)^2}{2|\boldsymbol{\xi}|^2}\,\mathrm{dV}_{\mathbf{x}'}\,\mathrm{d}t\,\mathrm{dV}_\mathbf{x} = \frac{1}{2}\int\limits_\Omega \int\limits_t \omega\phi\,\mathrm{d}t\,\mathrm{dV}_\mathbf{x} \tag{10}$$

[1] A piezoresistive behavior could be modeled considering the electrical microconductivity k_e function of an elastic deformation measure [34].

Eq. 10 has to be valid at any point of the domain Ω and at any time t. Hence, from Eq. 10 the indefinite equilibrium equation in steady-state conditions at $\mathbf{x}$ is set

$$\int_{H_{\mathbf{x}}} \frac{k_e(\phi' - \phi)}{|\boldsymbol{\xi}|^2} \, \mathrm{d}V_{\mathbf{x}} - \omega(\mathbf{x}, t) = 0 \tag{11}$$

Being $\boldsymbol{\xi} = \mathbf{x}' - \mathbf{x}$, we can write

$$\frac{k_e(\phi' - \phi)}{|\boldsymbol{\xi}|^2} = f_I(\mathbf{x}, \mathbf{x}', \phi, \phi') = f_I(\phi' - \phi, |\mathbf{x}' - \mathbf{x}|) \tag{12}$$

Thus, considering Eq. 1, it is demonstrated that the functional f_I depends upon the magnitude of the vector $\mathbf{x}' - \mathbf{x}$ and not upon its direction.
Adopting a meshfree discretization approach, the domain occupied by the body Ω is divided into a set of finite sub-volumes associated to each particle i. Then, a neighboring search algorithm selects particles j belonging to H_i according to the one-point quadrature scheme described Hu et al. [36, 37] that accounts for partial neighbor intersections.
The discretized form of the integral balance equation in steady-state regime is:

$$\sum_{j=1} f_I(\mathbf{x}^i, \mathbf{x}^j, \phi^i, \phi^j) \Delta V_j + \omega_i = 0 \tag{13}$$

where subscript j denotes a particle within the horizon region of particle i. Thus the sum in Eq. (13) is over all nodes j such that $|\mathbf{x}_j - \mathbf{x}_i| \leq \delta$ (i.e. neighboring particles of particle i).
Being the primary field of the electrical model the particles electric field potential, for a couple of connected particles (see Fig. 1) we can define $\{\phi\}$ and $\{f_I^*\}$ as

$$\{\phi\} = \{\phi^i \quad \phi^j\}^T; \qquad \{f_I^*\} = \{f_I^i \quad f_I^j\}^T \tag{14}$$

where $\{f_I^*\}$ is the vector of external actions in the electrical conduction model.
The compatibility equation relating the particles primary field ϕ to the magnitude of the bond electrical field e is instead

$$e = \{b\}^T\{\phi\} \longrightarrow \{b\}^T = -\frac{1}{|\boldsymbol{\xi}|}\{-1 \quad 1\} \tag{15}$$

The discrete form of the balance of the variation of the macroelectrical energy per unit time and the external electrical work per unit time of the interaction between particles i and j can then be written as

$$\frac{1}{2}\{\phi\}^T \frac{1}{2}\alpha \Delta V_i \Delta V_j \{b\} k_e \{b\}^T \{\phi\} = \frac{1}{2}\{\phi\}^T \{f_I^*\} \tag{16}$$

which leads to the linear system $[\mathcal{K}]_e\{\phi\} = \{f_I^*\}$, and then to the expression of the pairwise equivalent stiffness operator corresponding to a half interaction

$$[\mathcal{K}]_e = \frac{1}{2}\alpha \Delta V_i \Delta V_j \{b\} k_e \{b\}^T \tag{17}$$

α is the volume correction coefficient that takes into account the partial neighbor intersection [38]. The global matrix is given by

$$[\mathcal{K}]_E = \sum_{j=i} \sum_{j=1} [\mathcal{K}]_e^{ij} \tag{18}$$

It can be noted that in Eq.6, the factor 1/2 is included because the energy stored in each bond is associated equally with the two particles connected by the ligament. In the present implementation, the volume method for correcting the peridynamic surface effect is adopted [39].

2.1. Micro-conductivities

In the classical theory of homogenized elastic orthotropic materials, the electrical conductivity typically exhibits a directional dependent variation, whereas the current density vector is not necessarily parallel to the electric field. The relationship between the orthogonal components of the current density and the electrical field in the principal material system, inclined at angle ζ with respect to the horizontal, is given by

$$\boldsymbol{q_I} = \boldsymbol{D_e}\boldsymbol{e} \longrightarrow \left\{ \begin{array}{c} q_{I_1} \\ q_{I_1} \end{array} \right\} = \left[\begin{array}{cc} K_{e_{11}} & 0 \\ 0 & K_{e_{22}} \end{array} \right] \left\{ \begin{array}{c} e_1 \\ e_2 \end{array} \right\} \tag{19}$$

In Eq. 19, $\boldsymbol{D_e}$ is symmetric, second-rank tensors called electrical conductivity tensor of components $K_{e_{ii}}$.
Assuming here for simplicity that $\zeta = 0$, and considering an arbitrary coordinate system $\tilde{x}, \tilde{y}$ related to an orthonormal basis rotated by ψ with respect to the horizontal, Eq.(19) can be rewritten as

$$\tilde{\boldsymbol{q}}_{\boldsymbol{I}} = \tilde{\boldsymbol{D}}_{\boldsymbol{e}}\tilde{\boldsymbol{e}} \tag{20}$$

being $\tilde{\boldsymbol{D}}_{\boldsymbol{e}}$ defined as

$$\tilde{\boldsymbol{D}}_{\boldsymbol{e}} = \left[\begin{array}{cc} K_{e_{\tilde{x}\tilde{x}}} & K_{e_{\tilde{x}\tilde{y}}} \\ K_{e_{\tilde{x}\tilde{y}}} & K_{e_{\tilde{y}\tilde{y}}} \end{array} \right] = \mathbf{Q}_e \boldsymbol{D_e} \mathbf{Q}_e^T = \mathbf{Q}_e \left[\begin{array}{cc} K_{e_{11}} & 0 \\ 0 & K_{e_{22}} \end{array} \right] \mathbf{Q}_e^T \tag{21}$$

where $\mathbf{Q}_e$ is

$$\mathbf{Q}_e = \left[\begin{array}{cc} \cos\psi & -\sin\psi \\ \sin\psi & \cos\psi \end{array} \right] \tag{22}$$

The off-axis conductivity $K_{e_{\tilde{x}\tilde{x}}}$ can be written as function of the direction defined by angle ψ, and in terms of the two material constants defined in Eq. (19) as

$$K_{e_{\tilde{x}\tilde{x}}}(\psi) = K_{e_{11}}\cos^2\psi + K_{\mathrm{e}_{22}}\sin^2\psi \tag{23}$$

By analogy with the phenomenological classical description of anisotropic conductivity, we can assume for instance that the ligament microconductivity k_e is function of ψ (the bond inclination angle) as $K_{e_{\tilde{x}\tilde{x}}}$ described by Eq 23, namely

$$k_e(\psi) = k_{e_1}\cos^2\psi + k_{\mathrm{e}_2}\sin^2\psi \tag{24}$$

where k_{e_1} and k_{e_2} are the peridynamic inelastic micromoduli along the principal material axes. Thus, two independent microconductivities are defined for describing the conductive behavior of a two-dimensional orthotropic solid.
The relationship between the aforementioned microelectrical constants k_{e_1} and k_{e_2} of the proposed model and the conventional orthotropic continuum parameters can be obtained by equating the energy flow density per unit volume (namely the macroelectrical power density) of the proposed model and classical continuum for a general homogeneous electric field, which is

$$P_E(\mathbf{x}) = \frac{1}{2}\boldsymbol{e}\cdot\boldsymbol{q_I} = \frac{1}{2}\left[\begin{array}{cc} K_{e_{11}} & 0 \\ 0 & K_{e_{22}} \end{array} \right] \left\{ \begin{array}{c} e_1 \\ e_2 \end{array} \right\} \cdot \left\{ \begin{array}{c} e_1 \\ e_2 \end{array} \right\} = \frac{1}{2}(K_{e11}e_1^2 + K_{e22}e_2^2) \tag{25}$$

The corresponding quantity of the proposed model is instead given by the general integral

$$P_e(\mathbf{x}) = \frac{1}{2}\int\limits_{H_{\mathbf{x}}} \mathrm{w}_e \,\mathrm{dV}_{\mathbf{x}'} = \frac{1}{2}\int\limits_{H_{\mathbf{x}}} \frac{k_e(\psi)e^2(\psi)}{2}\,\mathrm{d}V_{\mathbf{x}'} = \frac{1}{2}\int\limits_{H_{\mathbf{x}}} \frac{k_e(\psi)(e_1\cos\psi + \mathrm{e}_2\sin\psi)^2}{2}\,\mathrm{d}V_{\mathbf{x}'} \tag{26}$$

in which, assuming $k_e(\psi)$ described by Eq. 24, leads to

$$P_e(\mathbf{x}) = \frac{1}{32}[e_1^2(3k_{e1} + k_{e2}) + e_2^2(k_{e1} + 3k_{e2})]\delta^2\pi h \tag{27}$$

where h is the thickness. Hence, comparing Eqs. 25 and 27, and collecting the terms that multiply the same electric field components, we obtain the system of two equations $W_E(\mathbf{x})_i = \Phi(\mathbf{x})_i$, $i = 1...2$

$$\begin{cases} \delta^2(3k_{e1} + k_{e2})\pi h = 16K_{e11} \\ \delta^2(k_{e1} + 3k_{e2})\pi h = 16K_{e22} \end{cases} \tag{28}$$

which provides

$$k_{e1} = \frac{2(3K_{e11} - K_{e22})}{\pi h\delta^2}; \qquad k_{e2} = \frac{2(3K_{e22} - K_{e11})}{\pi h\delta^2} \tag{29}$$

In the special case of isotropy we have $K_{e11} = K_{e22} = K_e$. Hence $k_{e1} = k_{e2} = k_e$, where

$$k_e = \frac{4K_e}{\pi h\delta^2} \tag{30}$$

which is the same expression of k_e for isotropic materials derived in [19, 34].
It should be noted that k_{e1} and k_{e2} can be considered general inelastic equivalent stiffness k_{ei}, $i = 1, 2$, of the non-local conductive micro-model. The macroscopic anisotropic conductive behavior is then the result of the microconductive properties assigned to the pairwise interactions. It should be noted that this mechanistic description of the directional dependency of the electrical conductivity, could be very useful to design real lattice materials with specific effective macroscopic anisotropic properties.
The micro-conductive parameters can satisfy the condition $k_{ei} > 0$, $k_{ei} < 0$, or $k_{ei} = 0$. If $k_{ei} < 0$, $\boldsymbol{q_I}$ and $\boldsymbol{e}$ in Eq. 2 would have opposite direction. In any case, negative parameters can introduce material instability, especially in presence of non-linearities. The choice of adopting Eq. 24 for describing the orientation dependence of the ligament conductivity parameter, is based on the specific assumption of trigonometric dependency of $k_e(\psi)$ on ψ, which is similar to that of $K_{e_{\tilde{x}\tilde{x}}}$ (i.e. Eq. 23). Actually, other laws of variation of the bond inelastic modulus with respect to the ligament inclination angle can be assumed. For instance, a more general description of $k_e(\psi)$ as function of the ligament orientation is

$$k_e(\psi) = k_{e_2} + (k_{e_1} - k_{e_2})\cos^n\psi \tag{31}$$

where $n = 2N$, with $N \subseteq \mathbb{N}^+$ (Eq. 24 is got assuming $n = 2$ in Eq. 31). The higher is the value of n, the higher is the degree of anisotropy of $k_e(\psi)$, whose coefficients k_{e1} and k_{e2} have to be calculated, as usual, to reproduce the conductive properties of a material. Hence, following one of the two analytical procedures descried in this section for deriving the micro-conductivities k_{e1} and k_{e2}, it is found that n allows for modeling materials with various levels of anisotropy, as it leads to non-negative micro-conductivities for $K_{e11}/K_{e22} \leq n + 1$. As an example, assuming n=4 and then solving Eq. 27 we obtain

$$k_{e1} = \frac{7K_{e11} - 3K_{e22}}{\pi h\delta^2}; \qquad k_{e2} = \frac{5K_{e22} - K_{e11}}{\pi h\delta^2} \tag{32}$$

whereas for $n = 12$ is

$$k_{e1} = \frac{991K_{e11} - 595K_{e22}}{99\pi h\delta^2}; \qquad k_{e2} = \frac{13K_{e22} - K_{e11}}{3\pi h\delta^2} \tag{33}$$

Hence, adopting Eqs. 32 and 33 together with Eq. 31 it is possible to model the conductive anisotropy of a material characterized by K_{e11}/K_{e22} up to 5 and 13, respectively, avoiding negative inelastic stiffness. Besides, all these configurations lead, in principle, to the same results since the corresponding parameters k_{e1} and k_{e2} are calculated analytically to match the effective anisotropic conductivity of the material. By increasing n for a given anisotropic ratio K_{e11}/K_{e22}, a progressively less smooth transition between the two values of micro-conductivities k_{e1} and k_{e2} is obtained. For this reason, when considering discrete array of particles instead of material points in a continuum, n should not be too large with respect to K_{e11}/K_{e22} for a given $m = \delta/\Delta x$, in such a way to reduce mesh dependency of the results. Another consideration is when $n = 2$ in Eq. 31. The law of variation of $k_e(\psi)$ is similar to that proposed for the elastic axial bond stiffness in classical bond-based orthotropic elastic models based on central pair potentials, and then characterized by two independent elastic parameters [27, 40]. Moreover, it can be demonstrated that the eight-order spherical harmonic expansion proposed in [27] for elasticity, is a special case of the proposed two parameters anisotropic function by setting $n = 12$ in Eq. 31.
When principal material directions are not aligned with the horizontal and vertical directions, (being $\zeta \neq 0$), Eq. 31 can be rewritten as

$$k_e(\psi, \zeta) = k_{e_2} + (k_{e_1} - k_{e_2})\cos^n(\psi - \zeta) \tag{34}$$

3. The micropolar mechanical model

The linear and angular momentum equilibrium equations in elastostatics of a two-dimensional continuum whose oriented material points within the distance δ, interact through non-central pair potentials [5, 14, 32] are

$$\int_{H_{\mathbf{x}}} \mathbf{f}(\mathbf{x}, \mathbf{x}', \mathbf{u}, \mathbf{u}', \theta, \theta')dV_{\mathbf{x}'} + \mathbf{b}(\mathbf{x}, t) = \mathbf{0} \quad \text{for} \quad \mathbf{x} \in \Omega, \tag{35}$$

$$\int_{H_{\mathbf{x}}} \mathsf{m}(\mathbf{x}, \mathbf{x}', \mathbf{u}, \mathbf{u}', \theta, \theta')dV_{\mathbf{x}'} + c(\mathbf{x}, t) = 0 \quad \text{for} \quad \mathbf{x} \in \Omega, \tag{36}$$

where, as in Eq.1 of Section 2, Ω is the domain occupied by the body, and $H_{\mathbf{x}}$ defines the horizon region of radius δ [6]. The applied body forces and couples are $\mathbf{b}$ and c, while $\mathbf{f}$ and m are the pairwise forces function and micromoment functions, respectively. In Eqs. 35-36 $\mathbf{u}' = \mathbf{u}(\mathbf{x}')$, $\mathbf{u} = \mathbf{u}(\mathbf{x})$, $\theta' = \theta(\mathbf{x}')$ and $\theta = \theta(\mathbf{x})$. In what follows, the vector $\mathbf{u}' - \mathbf{u} = \boldsymbol{\eta}$ denotes the relative displacement between the oriented material points $\mathbf{x}$ and $\mathbf{x}'$, respectively. The mechanical model is based on the definition of three linearized pairwise deformation measures that can be independently defined as functions of the displacements and rotations of a couple of interacting oriented material points. The deformation in the direction of the material points' joining line is the stretch s,

$$s = \frac{1}{|\boldsymbol{\xi}|}\left(\boldsymbol{\eta} \cdot \frac{\boldsymbol{\xi}}{|\boldsymbol{\xi}|}\right) = \frac{\eta_{\mathrm{n}}}{|\boldsymbol{\xi}|} = \frac{(u'_{\mathrm{n}} - u_{\mathrm{n}})}{|\boldsymbol{\xi}|} \tag{37}$$

where η_{n} is the component of $\boldsymbol{\eta}$ along the undeformed bond of unit vector $\boldsymbol{\xi}/|\boldsymbol{\xi}| = \mathbf{n}$. The shearing deformation is defined as the difference between the rotation angle of the ligament and the particles' average rotation

$$\gamma = \frac{\eta_{\mathrm{t}}}{|\boldsymbol{\xi}|} - \bar{\theta} = \frac{(u'_{\mathrm{t}} - u_{\mathrm{t}})}{|\boldsymbol{\xi}|} - \frac{(\theta' + \theta)}{2} \tag{38}$$

where η_{t} is the component of $\boldsymbol{\eta}$ along the direction $\mathbf{t}$ orthogonal to $\mathbf{n}$ The third pairwise deformation measure is function of the relative particles' rotation $\vartheta = \theta' - \theta$ and is here defined as $\chi = \vartheta/|\boldsymbol{\xi}|$.
The mechanical non-central interactions between pair or particles can be derived from the definition of a differentiable scalar-valued potential function

$$\mathrm{w} = (\mathrm{w_s} + \mathrm{w}_\gamma + \mathrm{w}_\vartheta) = \frac{k_{\mathrm{n}} s^2 |\boldsymbol{\xi}|}{2} + \frac{k_{\mathrm{t}} \gamma^2 |\boldsymbol{\xi}|}{2} + \frac{k_\chi \chi^2 |\boldsymbol{\xi}|}{2} \tag{39}$$

where $k_{\mathrm{n}}, k_{\mathrm{t}}$ and k_χ are the micro constitutive parameters related to the pairwise deformation measures defined s, γ and χ. As in [41, 33], being the attention here focused on Cauchy materials, the definition of a rotational stiffness is not strictly required, and is given here only for the sake of completeness. The first derivative of the potential function w (namely the micropotential energy function) gives

$$f_{\mathrm{n}} = \frac{\partial \mathrm{w_s}}{\partial \eta_{\mathrm{n}}}; \qquad f_{\mathrm{t}} = \frac{\partial \mathrm{w}_\gamma}{\partial \eta_{\mathrm{t}}}; \qquad \mathsf{m}_\vartheta = \frac{\partial \mathrm{w}_\vartheta}{\partial \vartheta} \tag{40}$$

Eqs. 39-40 state that the material is conservative (satisfies the conditions of microelasticity [6]), and each pair of material points $\mathbf{x}$ and $\mathbf{x}'$ interact through pairwise potentials or elastic springs whose reaction forces depend on deformation of the ligament.
The general form of the elastic energy per unit volume in the body $\Phi(\mathbf{x})$, namely the macroelastic energy density for the proposed model, is obtained by considering the force and couple components in Eq. 47 and their work-conjugate ligament deformation measures

$$\Phi(\mathbf{x}) = \frac{1}{2} \int_{H_{\mathbf{x}}} \mathrm{w} \, dV_{\mathbf{x}'} = \frac{1}{2} \int_{H_{\mathbf{x}}} \left\{ \frac{k_{\mathrm{n}} s^2 |\boldsymbol{\xi}|}{2} + \frac{k_{\mathrm{t}} \gamma^2 |\boldsymbol{\xi}|}{2} + \frac{k_\chi \chi^2 |\boldsymbol{\xi}|}{2} \right\} dV_{\mathbf{x}'} \tag{41}$$

The total macroelastic energy of the body is then given by

$$\hat{\Phi} = \frac{1}{2} \int_{\Omega} \int_{H_{\mathbf{x}}} \left\{ \frac{k_{\mathrm{n}} s^2 |\boldsymbol{\xi}|}{2} + \frac{k_{\mathrm{t}} \gamma^2 |\boldsymbol{\xi}|}{2} + \frac{k_\chi \chi^2 |\boldsymbol{\xi}|}{2} \right\} dV_{\mathbf{x}'} dV_{\mathbf{x}} \tag{42}$$

The discretized form of the linear and angular momentum equilibrium equations is:

$$\sum_{j=1} \mathbf{f}(\mathbf{x}^i, \mathbf{x}^j, \mathbf{u}^i, \mathbf{u}^j) \Delta V_j + \mathbf{b}_i = \mathbf{0}; \qquad \sum_{j=1} \mathsf{m}(\mathbf{x}^i, \mathbf{x}^j, \mathbf{u}^i, \mathbf{u}^j) \Delta V_j + c_i = 0 \tag{43}$$

where subscript j denotes a particle within the horizon region of particle i.
The particles forces, couples and displacements corresponding to each interaction in a local coordinate system are described by

$$\{f\}^T = \{f_{\mathrm{n}}^i \quad f_{\mathrm{t}}^i \quad \mathsf{m}^i \quad f_{\mathrm{n}}^j \quad f_{\mathrm{t}}^j \quad \mathsf{m}^j\}; \quad \{u\}^T = \{u_{\mathrm{n}}^i \quad u_{\mathrm{t}}^i \quad \theta^i \quad u_{\mathrm{n}}^j \quad u_{\mathrm{t}}^j \quad \theta^j\} \tag{44}$$

The ligament compatibility equation of the discretized system can be written in a compact form as

$$\{h\} = [B]\{u\} \tag{45}$$

hence

$$\{s \quad \gamma \quad \chi\}^T = \frac{1}{|\boldsymbol{\xi}|} \begin{bmatrix} -1 & 0 & 0 & 1 & 0 & 0 \\ 0 & -1 & -|\boldsymbol{\xi}|/2 & 0 & 1 & -|\boldsymbol{\xi}|/2 \\ 0 & 0 & -1 & 0 & 0 & 1 \end{bmatrix} \{u\} \tag{46}$$

The constitutive equation of the model can be written in matrix form as

$$\{q\} = [D]\{h\} \longrightarrow \{f_{\mathrm{n}} \quad f_{\mathrm{t}} \quad \mathsf{m}_\vartheta\}^T = \mathrm{diag}\{k_{\mathrm{n}} \quad k_{\mathrm{t}} \quad k_\chi\}\{s \quad \gamma \quad \chi\}^T \tag{47}$$

where $[D]$ is a diagonal matrix characterizing the elastic behavior of each ligament. It relates the pairwise actions and deformations measures of a couple of particles and is also function on the ligament orientation angle ψ in the case of non-isotropic elasticity. Note that m_ϑ represents only the self-equilibrated part of the particles couples m referred to a specific interaction.
It is worth underlying that the rotational spring allows the proposed formulation to be extended to micropolar elasticity. Actually, k_χ is independent of the other stiffness parameters and introduces an additional internal length into the model proper of micropolar continua [35]. Hence, considering a single interaction between two particles i and j, the discrete form of the balance of the variation of the total macroelastic energy and the work W done by the external nodal forces $\{p\}$ is

$$\hat{\Phi} = \frac{1}{2}\{u\}^T\frac{1}{2}[B]^T[D]\xi\Delta V_i\alpha\Delta V_j[B]\{u\} = \frac{1}{2}\{u\}^T\{p\} = W \tag{48}$$

where $\xi = |\boldsymbol{\xi}|$.
The half ligament elastic pairwise stiffness operator in the global coordinate system can then be expressed by

$$[\mathcal{K}]_{el} = \frac{1}{2}\alpha\Delta V_i\Delta V_j[R]^T[B][D]\xi[B]^T[R] \tag{49}$$

where $[R]$ is the rotation matrix [5] and where the factor $1/2$ is due to the definition of the macroelastic energy density function.
The classical constitutive equation of an in-plane orthotropic material in the material reference system inclined at angle ζ with respect to the horizontal can be written using Voigt notation as:

$$\boldsymbol{\sigma} = \mathbf{C}\boldsymbol{\epsilon} \longrightarrow \left\{ \begin{array}{c} \sigma_{11} \\ \sigma_{22} \\ \tau_{12} \end{array} \right\} = \left[\begin{array}{ccc} C_{11} & C_{12} & 0 \\ C_{12} & C_{22} & 0 \\ 0 & 0 & C_{66} \end{array} \right] \left\{ \begin{array}{c} \epsilon_{11} \\ \epsilon_{22} \\ 2\epsilon_{12} \end{array} \right\} \tag{50}$$

Assuming first, for simplicity that $\zeta = 0$, and considering a generic coordinate system $\tilde{x}, \tilde{y}$ related to an orthonormal basis rotated by ψ with respect to the horizontal, Eq.(50) can be rewritten as

$$\tilde{\boldsymbol{\sigma}} = \tilde{\mathbf{C}}\tilde{\boldsymbol{\epsilon}} \tag{51}$$

being $\tilde{\mathbf{C}}$ defined as

$$\tilde{\mathbf{C}} = \left[\begin{array}{ccc} C_{\tilde{x}\tilde{x}} & C_{\tilde{x}\tilde{y}} & C_{\tilde{x}\tilde{s}} \\ C_{\tilde{x}\tilde{y}} & C_{\tilde{y}\tilde{y}} & C_{\tilde{y}\tilde{s}} \\ C_{\tilde{x}\tilde{s}} & C_{\tilde{y}\tilde{s}} & C_{\tilde{s}\tilde{s}} \end{array} \right] = \mathbf{Q}\mathbf{C}\mathbf{Q}^T = \mathbf{Q}\left[\begin{array}{ccc} C_{11} & C_{12} & 0 \\ C_{12} & C_{22} & 0 \\ 0 & 0 & C_{66} \end{array} \right]\mathbf{Q}^T \tag{52}$$

where $\mathbf{Q}$ is the transformation matrix [33].
According to Eq. 52, the off-axis axial $C_{\tilde{x}\tilde{x}}$ and shear $C_{\tilde{s}\tilde{s}}$ moduli can be written as function of ψ, in terms of the four material constants C_{11}, C_{12}, C_{22} and C_{66} that define in-plane orthotropy

$$C_{\tilde{x}\tilde{x}}(\psi) = C_{11}\cos^4\psi + C_{22}\sin^4\psi + 2C_{12}\sin^2\psi\cos^2\psi + 4C_{66}\sin^2\psi\cos^2\psi \tag{53}$$

$$C_{\tilde{s}\tilde{s}}(\psi) = C_{11}\sin^2\psi\cos^2\psi + C_{22}\sin^2\psi\cos^2\psi - 2C_{12}\sin^2\psi\cos^2\psi + C_{66}(\cos^2\psi - \sin^2\psi)^2 \tag{54}$$

In order to preserve the material symmetry, and in analogy with the classical continuum, we assume that in our model the axial and shear ligament stiffness (i.e.k_{n} and k_{t}) have a directional dependency similar to that of $C_{\tilde{x}\tilde{x}}$ and $C_{\tilde{s}\tilde{s}}$ described by Eqs.53-54, respectively

$$k_{\mathrm{n}}(\psi) = k_{\mathrm{n}_1}\cos^4\psi + k_{\mathrm{n}_2}\sin^4\psi + 2k_v\sin^2\psi\cos^2\psi + 4k_{\mathfrak{t}}\sin^2\psi\cos^2\psi \tag{55}$$

$$\begin{aligned} k_{\mathrm{t}}(\psi) = {} & k_{\mathrm{n}_1}\sin^2\psi\cos^2\psi + k_{\mathrm{n}_2}\sin^2\psi\cos^2\psi - 2k_v\sin^2\psi\cos^2\psi \\ & + k_{\mathfrak{t}}(\cos^2\psi - \sin^2\psi)^2 \end{aligned} \tag{56}$$

where k_{n_1} and k_{n_2} are the axial micromoduli along principal material axes, $k_{\mathrm{t}_1} = k_{\mathrm{t}_2} = k_{\mathfrak{t}}$ is the shear micromodulus along the principal material axis and k_v is related to the ratio between $k_{\mathrm{t}}(\psi)$ and $k_{\mathrm{n}}(\psi)$ in each ligament direction. The relation between the orthotropic microelastic moduli, k_{n_1}, k_{n_2}, k_v and $k_{\mathfrak{t}}$ and the classical continuum elastic constants in Eq.50, is obtained following a general approach based on energetic equivalence without the need for any particular assumption about the deformation fields, and similar to that used in 2.1 for the micro-conductivities.

Considering a general two-dimensional homogeneous deformation field of components ϵ_{11}, ϵ_{22} and ϵ_{12}, the strain energy density of the classical Cauchy linear elastic orthotropic continuum is

$$\varphi(\mathbf{x}) = \frac{1}{2}(C_{11}\epsilon_{11}^2 + C_{22}\epsilon_{22}^2 + 2C_{12}\epsilon_{11}\epsilon_{22} + 4G_{66}\epsilon_{12}^2) \tag{57}$$

The corresponding quantity of the proposed model is instead given by the general integral [2]

$$\Phi(\mathbf{x}) = \frac{1}{2}\int_{H_{\mathbf{x}}} \left\{ \frac{k_{\mathrm{n}}(\psi)s^2(\psi)|\boldsymbol{\xi}|}{2} + \frac{k_{\mathrm{t}}(\psi)\gamma^2(\psi)|\boldsymbol{\xi}|}{2} \right\} dV_{\mathbf{x}'} \tag{58}$$

in which, being the imposed deformation field affine, the deformation measures $s(\psi)$ and $\gamma(\psi)$ of a specific ligament inclined at ψ are related to the homogeneous strain components ϵ_{ij} through

$$s(\psi) = \epsilon_{11}\cos\psi^2 + \epsilon_{22}\sin\psi^2 + 2\epsilon_{12}\cos\psi\ \sin\ \psi \tag{59}$$

$$\gamma(\psi) = \epsilon_{12}(\cos\psi^2 - \sin\psi^2) + (\epsilon_{22} - \epsilon_{11})\cos\psi\ \sin\ \psi \tag{60}$$

Hence, in the case of classical homogeneous deformation, $s(\psi) = \epsilon_{\tilde{x}\tilde{x}}(\psi)$ and $\gamma(\psi) = 2\epsilon_{\tilde{x}\tilde{y}}(\psi) = \gamma^*_{\tilde{x}\tilde{y}}(\psi)$. Substituting Eqs. 59 and 60 in Eq. 58, and assuming $k_{\mathrm{n}}(\psi)$ and $k_{\mathrm{t}}(\psi)$ by Eqs. 55-56, the general solution of the integral in Eq. 58 is obtained

$$\Phi(\mathbf{x}) = \frac{\pi h\delta^3}{384}[\epsilon_{11}^2(19k_{\mathrm{n}_1} + 3k_{\mathrm{n}_2} + 12k_{\mathfrak{t}} + 2k_v) + \epsilon_{22}^2(3k_{\mathrm{n}_1} + 19k_{\mathrm{n}_2} + 12k_{\mathfrak{t}} + 2k_v) \tag{61}$$

$$+ 2\epsilon_{11}\epsilon_{22}(k_{\mathrm{n}_1} + k_{\mathrm{n}_2} + 4k_{\mathfrak{t}} + 6k_v) + 4\epsilon_{12}^2(3k_{\mathrm{n}_1} + 3k_{\mathrm{n}_2} + 12k_{\mathfrak{t}} + 2k_v)] \tag{62}$$

Comparing Eqs. 57 and 58, and collecting the terms that multiply the same strain components ϵ_{ij}, a system of four equations $\phi(\mathbf{x})_i = \Phi(\mathbf{x})_i$, $i = 1...4$ is obtained

$$\begin{cases} \frac{C_{11}}{2} = \frac{h\pi\delta^3}{384}(19k_{\mathrm{n}_1} + 3k_{\mathrm{n}_2} + 12k_{\mathfrak{t}} + 2k_v) \\ \frac{C_{22}}{2} = \frac{h\pi\delta^3}{384}(3k_{\mathrm{n}_1} + 19k_{\mathrm{n}_2} + 12k_{\mathfrak{t}} + 2k_v) \\ \frac{C_{12}}{2} = \frac{h\pi\delta^3}{384}(k_{\mathrm{n}_1} + k_{\mathrm{n}_2} + 4k_{\mathfrak{t}} + 6k_v) \\ \frac{C_{66}}{2} = \frac{h\pi\delta^3}{384}(3k_{\mathrm{n}_1} + 3k_{\mathrm{n}_2} + 12k_{\mathfrak{t}} + 2k_v) \end{cases} \tag{63}$$

[2] In the case of homogeneous deformation fields and when modeling Cauchy materials, the rotational degree of freedom is not activated, as shown in [5, 41].

whose solution gives

$$k_{\mathrm{n}_1} = \frac{12\,(C_{11} - C_{66})}{\pi h \delta^3}; \qquad k_{\mathrm{n}_2} = \frac{12\,(C_{22} - C_{66})}{\pi h \delta^3} \tag{64}$$

$$k_v = \frac{12\,(3C_{12} - C_{66})}{\pi h \delta^3}; \qquad k_{\mathtt{t}} = \frac{3\,(8C_{66} - C_{11} - C_{22} - 2C_{12})}{\pi h \delta^3} \tag{65}$$

In the case of isotropy, $C_{11} = C_{22}$ and $C_{12} = C_{11} - 2C_{66}$. Eqs. (64) and (65) provide two independent microelastic constants in terms of C_{11} and C_{66} only, as

$$k_{\mathrm{n}_1} = k_{\mathrm{n}_2} = k_n = \frac{12\,(C_{11} - C_{66})}{\pi h \delta^3}; \qquad k_{\mathtt{t}} = \frac{12\,(3C_{66} - C_{11})}{\pi h \delta^3}; \qquad k_v = k_{\mathrm{n}} - 2k_{\mathtt{t}} \tag{66}$$

Eqs. (55) and (56), define the values of the axial and shear microelastic stiffness at each ligament orientation ψ. In other words, two anisotropic elastic potentials are defined, and then two equivalent springs whose stiffness is continuous trigonometric functions of the bond orientation ψ and the four elastic material constants that define classical Cauchy orthotropic in-plane elasticity [41]. In the case of isotropic materials, the microelastic stiffnesses are independent on the orientation of the ligament, hence their values are uniform.

The proposed formulation, that is inspired by Voigt's molecular theory of elasticity [32], is micropolar in the sense that particles are characterized also by a rotational degree of freedom that is required to ensure rotational invariance of the model [5]. Being the pairwise forces not directed along the particles centroids joining line (non-central forces assumption [32]), rotations and hence micromoments ensure the balance of angular momentum of each ligament. As a consequence, the shear deformation measure introduced accounts for particle's rotations [5].

It should be reminded that the rotational spring constant k_χ is strictly related to a bending stiffness, and in the case of Cauchy materials should be, in general set to zero. When principal material system is not aligned with the horizontal, (being $\zeta \neq 0$), Eqs.(55) and (56) get the general form

$$\begin{aligned} k_{\mathrm{n}}(\psi,\zeta) = {} & k_{\mathrm{n}_1}\cos^4(\psi-\zeta) + k_{\mathrm{n}_2}\sin^4(\psi-\zeta) \\ & + 2k_v\sin^2(\psi-\zeta)\cos^2(\psi-\zeta) + 4k_{\mathtt{t}}\sin^2(\psi-\zeta)\cos^2(\psi-\zeta) \end{aligned} \tag{67}$$

$$\begin{aligned} k_{\mathrm{t}}(\psi,\zeta) = {} & k_{\mathrm{n}_1}\sin^2(\psi-\zeta)\cos^2(\psi-\zeta) + k_{\mathrm{n}_2}\sin^2(\psi-\zeta)\cos^2(\psi-\zeta) + \\ & - 2k_v\sin^2(\psi-\zeta)\cos^2(\psi-\zeta) + k_{\mathtt{t}}[\cos^2(\psi-\zeta) - \sin^2(\psi-\zeta)]^2 \end{aligned} \tag{68}$$

Hence, given a specific value of the angle ζ, $k_{\mathrm{n}} = k_{\mathrm{n}}(\psi,\zeta)$ and $k_{\mathrm{t}} = k_{\mathrm{t}}(\psi,\zeta)$ are obtained from Eqs 67-68.

3.1. An energetic failure criterion for orthotropic materials

An energetic failure criterion for orhotropic materials based on the definition of an orientation dependent critical value of the ligament stored energy is proposed. This criterion, firstly introduced by Foster et al. [42] for isotropic materials, then adapted to micropolar lattices by Diana and Ballarini [33] for modelling orthotropic materials with theoretically uniform fracture resistance, is here extended to the general case of anisotropic surface energy. The importance of considering an energetic failure criterion in micropolar lattice formulations for anisotropic materials relies on crack front which is in general locally associated to a mixed-mode deformation. Therefore, a classical critical elongation criterion is not, in general, recommended since

it does not take into account the shear deformation of the ligament. This aspect could lead, in principle, also to a non correct energy dissipation during crack extension. In fact, adopting a deformation (axial) based failure criterion, a limit value for the fiber elongation related to the mechanical behavior of the equivalent axial spring is considered. Nevertheless, in isotropic materials at atmospheric pressure, the crack front is locally associated with a mode I deformation leading to well simulated failure conditions and realistic crack paths using the critical elongation criterion even in the case of pure mode II external loading [43, 44, 45, 46, 7, 47, 48]. However, the situation is different in the case of anisotropic materials which need a lattice failure criterion accounting for shearing deformations to describe properly the crack nucleation and kinking phenomenon [33]. The here proposed energetic criterion considers the rupture of the bond when its stored energy, i.e. the elastic micropotential w reaches a critical value w_u. It takes into account both w_s (i.e. the micropotential energy function corresponding to the axial spring) and w_γ (i.e. the micropotential energy function corresponding the shear spring). It should be reminded that when modeling Cauchy materials, the rotational springs is not necessary and its value is here set equal to zero. Assuming that the surface energy is not uniform, the critical value of the ligament stored energy is not the same for each orientation ψ. The critical value w_u of the bond micropotential energy $\mathrm{w} = \mathrm{w}_s + \mathrm{w}_\gamma$ can be calculated setting the fracture energy of the material $G(\zeta)$, where ζ is the orientation of the material reference system, equal to the total work required to break all the bonds per unit of fracture surface, assumed here orthogonal to the horizontal (see Fig. 2)

$$G(\zeta) = \int_0^\delta \int_z^\delta \int_{-\cos^{-1}(z/|\boldsymbol{\xi}|)}^{\cos^{-1}(z/|\boldsymbol{\xi}|)} \mathrm{w}_u(\psi,\zeta)\, h|\boldsymbol{\xi}|\, \mathrm{d}\psi\, \mathrm{d}\xi\, \mathrm{d}z \tag{69}$$

Considering that experimental measures of the fracture energy of orthotropic materials is, in general, given for two orthogonal orientation of the material reference system $\zeta = 0$ and $\zeta = \pi/2$ (with $G_{\zeta=0} > G_{\zeta=\pi/2}$), $\mathrm{w_u}(\psi,\zeta)$ depends on the ligament orientation angle by a general two parameter law similar to Eqs. 70- 31

$$\mathrm{w}_u(\psi,\zeta) = \mathrm{w}_{u2} + (\mathrm{w}_{u1} - \mathrm{w}_{u2})\cos^n(\psi - \zeta) \tag{70}$$

By substituting Eq. 70 in Eq. 69 and considering $\zeta = 0$ and $\zeta = \pi/2$, a system of two integral equations is obtained

$$G_{\zeta=0} = \int_0^\delta \int_z^\delta \int_{-\cos^{-1}(z/|\boldsymbol{\xi}|)}^{\cos^{-1}(z/|\boldsymbol{\xi}|)} \left\{ \mathrm{w}_{u2} + (\mathrm{w}_{u1} - \mathrm{w}_{u2})\cos^n\psi \right\} h|\boldsymbol{\xi}|\, \mathrm{d}\psi\, \mathrm{d}\xi\, \mathrm{d}z \tag{71}$$

$$\begin{aligned} G_{\zeta=\pi/2} = \int_0^\delta \int_z^\delta \int_{-\cos^{-1}(z/|\boldsymbol{\xi}|)}^{\cos^{-1}(z/|\boldsymbol{\xi}|)} \Big\{ & \mathrm{w}_{u2} + (\mathrm{w}_{u1} - \mathrm{w}_{u2}) \\ & \times \cos^n(\psi - \pi/2) \Big\}\, h|\boldsymbol{\xi}|\, \mathrm{d}\psi\, \mathrm{d}\xi\, \mathrm{d}z \end{aligned} \tag{72}$$

Adopting $n = 2$, a system of two equations in the two unknown w_{u1} and w_{u2} can be derived solving Eqs. 71- 72

$$\begin{cases} 9G_{\zeta=0} = 2h\delta^3(2\mathrm{w}_{u1} + \mathrm{w}_{u2}) \\ 9G_{\zeta=\pi/2} = 2h\delta^3(\mathrm{w}_{u1} + 2\mathrm{w}_{u2}) \end{cases} \tag{73}$$

which results in

$$\mathrm{w}_{u1} = \frac{3(2G_{\zeta=0} - G_{\zeta=\pi/2})}{2h\delta^3}; \qquad \mathrm{w}_{u2} = \frac{3(2G_{\zeta=\pi/2} - G_{\zeta=0})}{2h\delta^3} \tag{74}$$

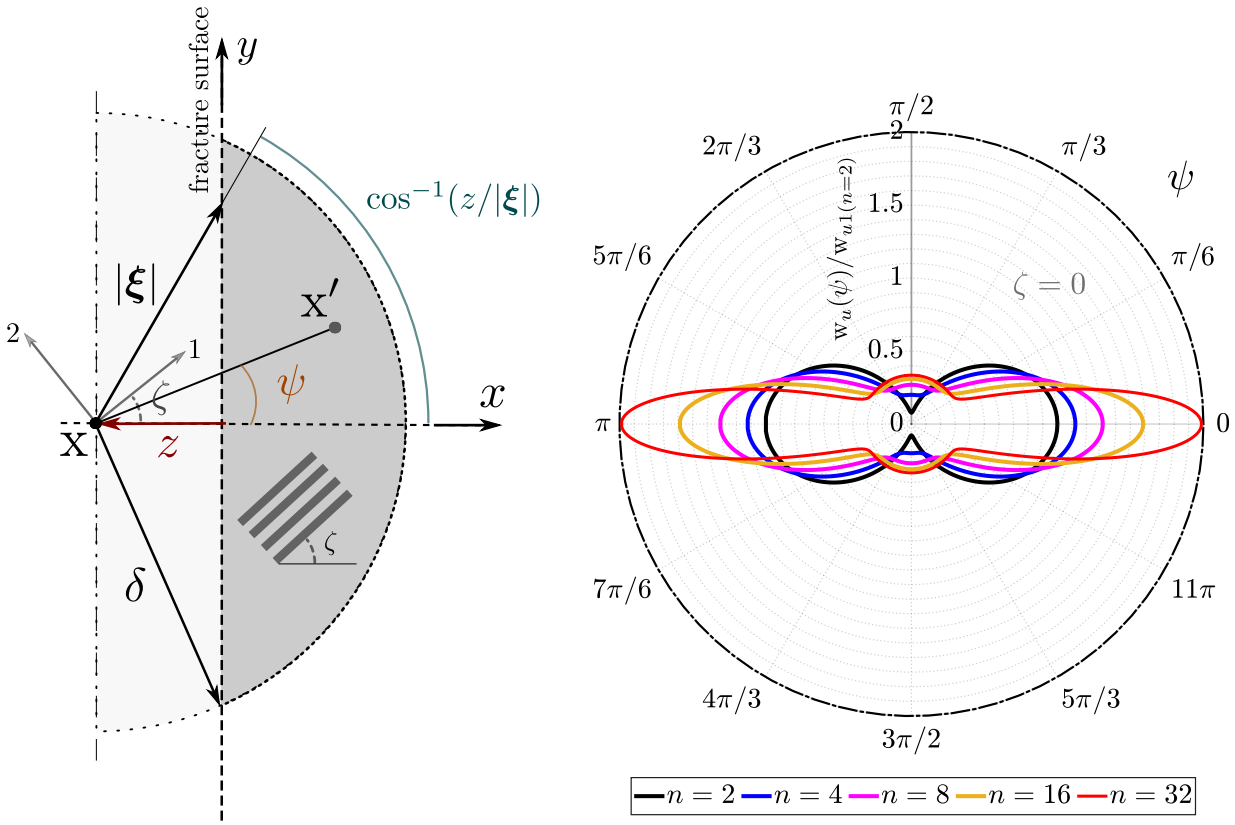

Figure 2: Schematics for computing the fracture energy of the material associated to a fracture plane orthogonal to the horizontal and corresponding to a specific orientation of the material reference system ζ (left); Continuous function $\mathrm{w}_u(\psi,\zeta)$ for a given material inclined at $\zeta = 0$, with $G_{\zeta=0}/G_{\zeta=\pi/2} = 1.8$ and corresponding to different values of the exponent n in Eq. 70 (right).

If instead, $n = 4$ and $n = 8$ are adopted in Eq. 70, Eqs. 71- 72 lead to the following relations

$$\mathrm{w}_{u1} = \frac{3(12G_{\zeta=0} - 7G_{\zeta=\pi/2})}{10h\delta^3}; \qquad \mathrm{w}_{u2} = \frac{3(8G_{\zeta=\pi/2} - 3G_{\zeta=0})}{10h\delta^3} \tag{75}$$

$$\mathrm{w}_{u1} = \frac{3(280G_{\zeta=0} - 187G_{\zeta=\pi/2})}{186h\delta^3}; \qquad \mathrm{w}_{u2} = \frac{3(128G_{\zeta=\pi/2} - 35G_{\zeta=0})}{186h\delta^3} \tag{76}$$

In the case of uniform fracture energy, $G_{\zeta=0} = G_{\zeta=\pi/2}$, Eqs. 74- 76 (same for any n) reduce to the well known [42, 33, 49]

$$\mathrm{w}_{u1} = \mathrm{w}_{u2} = \mathrm{w}_u = \frac{3G}{2h\delta^3} \tag{77}$$

being $\mathrm{w}_u(\psi,\zeta)$ a constant function. It is worth noting that w_{u1} and w_{u2} cannot be less than zero otherwise bond rupture generates energy, then a restriction exists on the maximum possible $G_{\zeta=0}/G_{\zeta=\pi/2}$ ratio corresponding to each value of the exponent n. Assuming for instance n=2 and n=8, the following restrictions hold $G_{\zeta=0} < 2G_{\zeta=\pi/2}$ and $G_{\zeta=0} < 3.65G_{\zeta=\pi/2}$, respectively. Therefore, n allows for modeling materials with various levels of anisotropy of the fracture resistance, as Eqn. 70, together with the corresponding values of w_1 and w_2, is able to model the failure behavior of materials characterized by $G_{\zeta=0}/G_{\zeta=\pi/2}$ up to 2 and 3.65, respectively. Increasing n for a given anisotropic ratio $G_{\zeta=0}/G_{\zeta=\pi/2}$, a progressively less smooth transition between the two values of micropotential energies w_{u1} and w_{u2} is obtained, as shown in Fig. 2. Hence, when considering a discretized model with a given $G_{\zeta=0}/G_{\zeta=\pi/2}$ ratio, higher exponent n values could require an higher value of the density parameter m for an accurate angular

discretization of the constitutive laws based on continuous trigonometric functions. In any case, w_{u1} and w_{u2} are calculated to match, for any values of n, the experimental fracture energy values of the material $G_{\zeta=0}$ and $G_{\zeta=\pi/2}$. However, since the integrals in Eqs. 71 and 72 are referred to specific orientations of the material reference system (or conversely, given $\zeta = 0$ 71 and 72 are associated with specific orientations of the fracture plane), the resulting fracture energy assumes transition values between $\zeta = 0$ and $\zeta = \pi/2$.
A similar conceptual idea can be found in phase-field formulations of anisotropic fracture, in which fracture anisotropy is modeled in a variational framework by considering an orientation dependent fracture energy G_ζ [50]. The convexity of the fracture energy decides the capability of the model to capture different types of anisotropy [50, 51]. However, phase-field models of fracture follow, in general, a phenomenological approach which allows to adopt directly a specific anisotropic surface energy, whereas in mechanistic models macroscopic anisotropic fracture properties are instead the result of micro-interaction failure properties.
An important aspect of the proposed energetic criterion, is that the failure properties of the model are independent of the elastic anisotropic properties. Hence, when equating the total work per unit of fracture surface and fracture energy of the material (i.e. Eq. 69), the integrals do not involve neither microelastic moduli, nor $k_{\mathrm{n}}(\psi)$ and $k_{\mathrm{t}}(\psi)$ functions, with consequent simplification of the calculation of the model critical parameters.
In order to specify the status of a specific bond $\boldsymbol{\xi}_{ij}$ connecting two particles $\mathbf{x}_i$ and $\mathbf{x}_j$, a history-dependent pairwise scalar valued function μ is introduced [40]

$$\mu(\boldsymbol{\xi}_{ij}, t) = \begin{cases} 0 & \mathrm{w} \geq \mathrm{w}_u \\ 1 & \mathrm{w} < \mathrm{w}_u \end{cases} \tag{78}$$

Then, a local damage variable is defined and computed at each pseudo-time step t and for each particle $\mathbf{x}_i$ as

$$d(\mathbf{x}_i, t) = 1 - \frac{\sum_{j=1} \mu(\boldsymbol{\xi}_{ij}, t) \Delta V_j}{\sum_{j=1} \Delta V_j} \tag{79}$$

where d is the point-wise local damage variable associated to the proposed failure criterion. It should be noted that in coupled-electro-mechanical formulations the ligament global stiffness is assembled as

$$[\mathcal{K}] = \mu\big[[\mathcal{K}]_e + [\mathcal{K}]_{el}\big] \tag{80}$$

hence, the pairwise scalar valued function μ affects also the conductivity of the ligament. In particular, when $\mu(\boldsymbol{\xi}_{ij}, t) = 0$, the ligament is no longer able to conduct electric current.

4. Validation of the model

The accuracy of the proposed formulation is illustrated by the simulation of: the effective conductive behavior and electric field potential in square laminae with homogenized anisotropic properties, the variation of electric resistance in a rectangular anisotropic specimen due to an evolving central crack (Section 4.1), and the fracture propagation and damage sensing in cortical

Table 1: Homogenized conductive properties of composite materials: Volume fraction V_f and electrical conductivities of the two phases fiber-matrix characterizing the three RVEs considered in this work.

MAT ID	K_e (Matrix) [S/mm]	$\beta = K_e$ (Fiber)$/K_e$ (Matrix)	$V_f = v_f/v$
1	100	10	0.50
2	20	50	0.50
3	1	1000	0.35

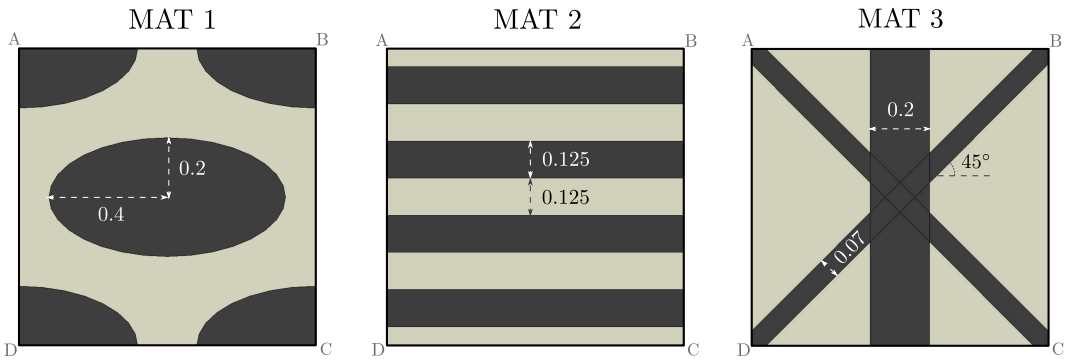

Figure 3: Homogenized conductive properties of composite materials: Schematics of the representative volume element (RVE) corresponding to the three 2D fiber composite materials considered (dimensions are related to the unit cell square side).

bone compact tensile test specimens considering different orientation of the material reference system (Section 4.2).

4.1. Anisotropic electrical conduction

The validation of the anisotropic conductive model has been conducted using three different in-plane effective anisotropic conductive properties resulting from an homogenization process of representative volume elements (RVE) and corresponding to three different two-phases inclusion (e.g. fiber)-matrix polymer composites.
Calculation of homogenized anisotropic conductivity tensors has been made using heterogeneous

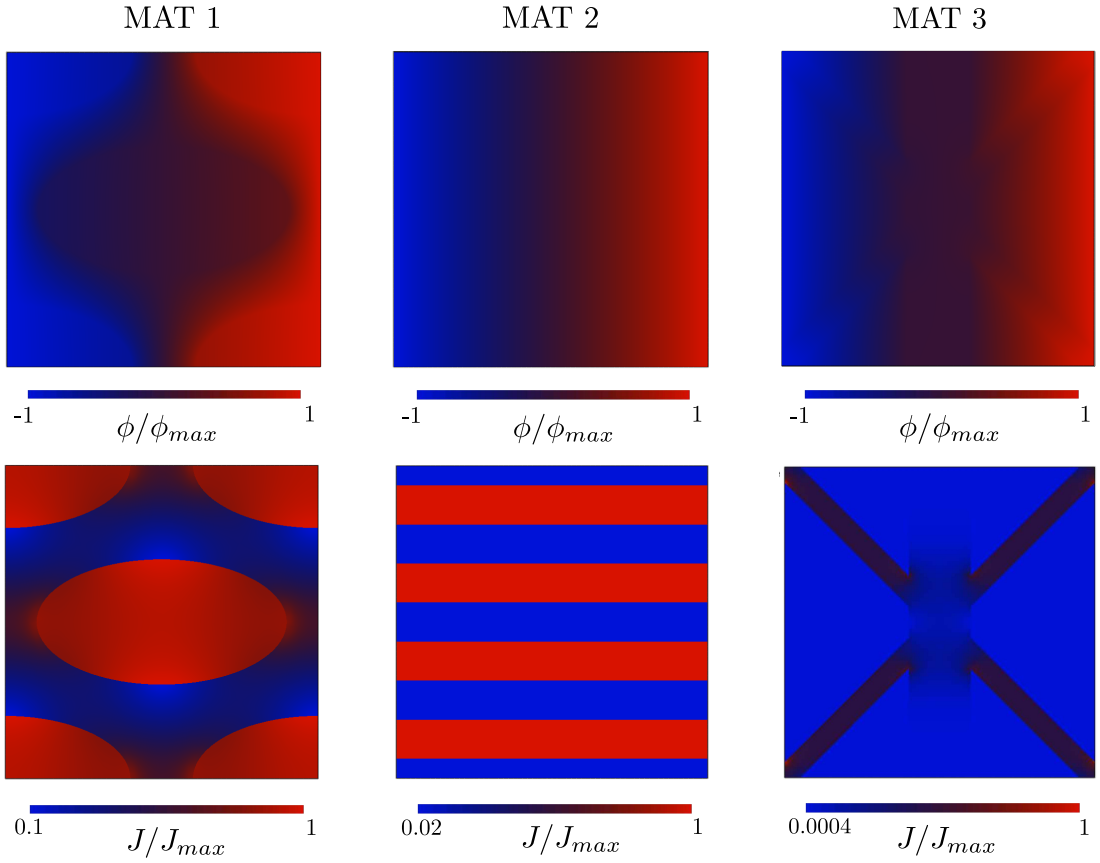

Figure 4: Normalized electric field potential ϕ/ϕ_{max} (top) and normalized electric current density J/J_{max} (bottom) for the three RVEs considered as result of $\Delta\phi(AD - BC)$.

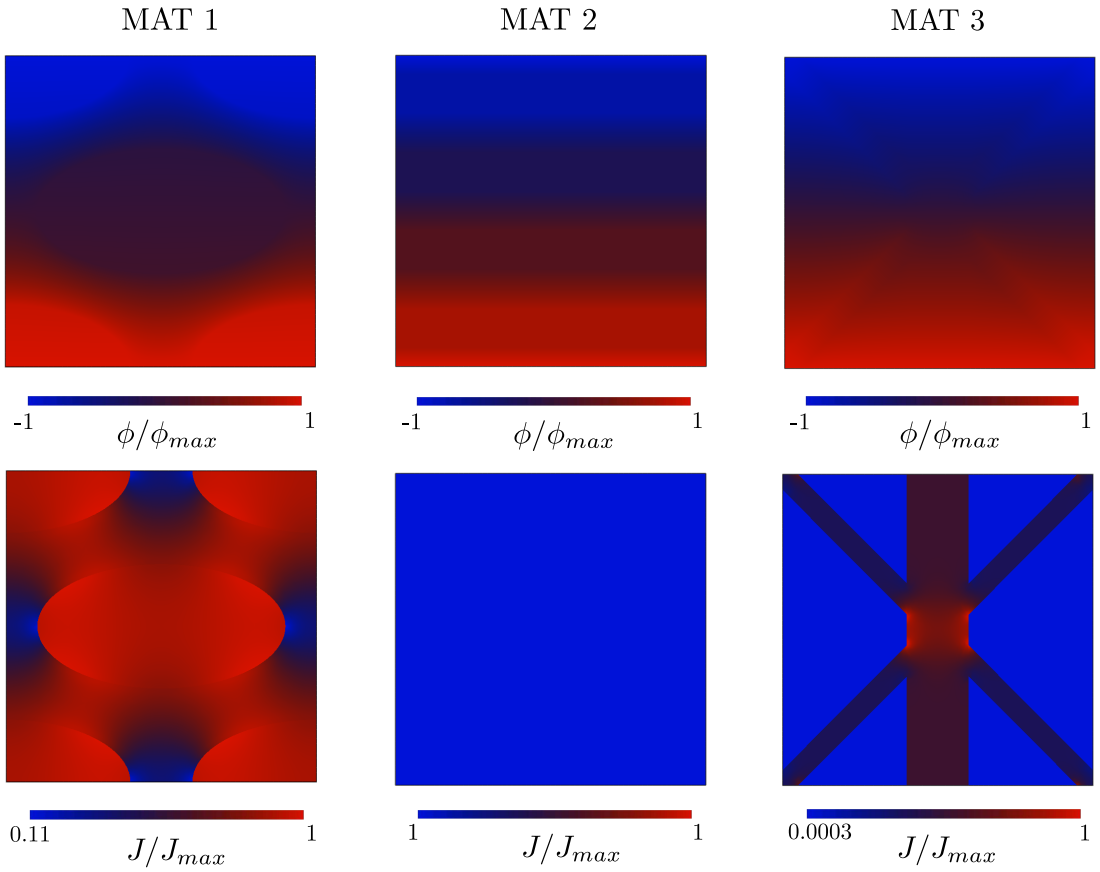

Figure 5: Normalized electric field potential ϕ/ϕ_{max} (top) and normalized electric current density J/J_{max} (bottom) for the three RVEs considered as result of $\Delta\phi(AB-CD)$.

finite element (FE) models in which matrix and inclusions are modeled as separate phases. For simplicity reasons, most micromechanical models assume a periodic arrangement of inclusions for which a RVE or unit cell can be isolated. The RVE is assumed to have unit thickness and the same volume fraction V_f as the composite. The three RVEs considered are described in Fig. 3 and the conductive isotropic properties adopted for each component (see Tab. 1) are compatible with a multitude of multi-phase polymer composites made of carbon fibers and polymer matrix with conductive fillers [52, 53].

Given two configurations of applied external potential difference at boundaries $\Delta\phi(AD-BC)$ and $\Delta\phi(AB-CD)$, and corresponding to macroscopic electric fields directed along the principal material directions [54], once the electric field potential is evaluated, the components K_{e_1} and K_{e_2} of the second rank effective conductivity tensor for each material are calculated by integrating the current density J across the boundaries AD and AB, respectively (see Figs. 4 and 5)

$$\bar{q}_{AD} = \frac{1}{S_{AD}} \int_S J \, \mathrm{d}S_{AD}; \qquad \bar{q}_{AB} = \frac{1}{S_{AB}} \int_S J \, \mathrm{d}S_{\mathrm{AB}} \tag{81}$$

where $\bar{q}_{AD}$ and $\bar{q}_{AB}$ are the macroscopic electric current fluxes (e.g. macroscopic current densities) on AD and AB, respectively. As consequence of the applied electric fields, the current density flows from the right to the left face in Fig. 4, and from the bottom to the top face in Fig. 5, being the remaining surfaces assumed to be electrically insulated [55, 56]. The electric current fluxes concentrate around the inclusions due to their higher conductivity properties. Hence, by solving the equations of the effective electrical conduction of the RVE

$$\bar{q}_1 = \bar{q}_{AD} = K_{e_1}[\Delta\phi(AD-BC)]; \qquad \bar{q}_2 = \bar{q}_{AB} = K_{e_2}[\Delta\phi(AB-CD)] \tag{82}$$

Table 2: Homogenized conductive properties of composite materials: Effective anisotropic homogenized electrical conductivities K_{e_1} [S/mm] and K_{e_2} [S/mm] corresponding to the three RVEs considered.

MAT ID	K_{e_1} [S/mm]	K_{e_2} [S/mm]	K_{e_1}/K_{e_2}
1	297	210	1.41
2	510	39.3	12.98
3	122	276	0.45

for K_{e_1} and K_{e_2}, the components of the effective conductivity tensor corresponding to the three RVEs considered (denoted by MAT 1, MAT 2 [3] and MAT 3) are reported in Tab. 2. It should be noted that only the diagonal terms of the conductivity tensor in the material reference system are non-zero for the RVEs. Composites with a non-orthogonal lattice of inclusions and not aligned anisotropy axes of phase materials are expected instead to possess macroscopic anisotropy of a general type [54]. Using the estimated effective conductivities of the composite materials considered, the microelectrical conductivity functions $k_e(\psi)$ characterizing the proposed model have been calculated by Eqs. 29, 33 and Eq. 31 (see Fig. 6 for details).
The accuracy of the proposed model is first assessed predicting the effective conductive behavior of a homogenized anisotropic material. To this purpose, a rectangular lamina of unitary thickness, length b=10mm, height $2b$=20mm and electrical conductive properties as those of MAT 2 ($K_{e_1} > 10K_{e_2}$) has been considered. A potential difference of $\Delta\phi$= 10 V is applied to the horizontal (top and bottom) boundaries, whereas the domain is discretized using different regular grid spacing $\Delta x = 0.5$ mm, $\Delta x = 0.25$ mm and $\Delta x = 0.125$ mm, resulting in a model composed of 800, 3200 and 12800 particles, respectively. The $\delta/\Delta x$=m density ratio is also varied to investigate the influence of the range of non-local actions on the model accuracy. Adopting four different orientation ζ of the material reference system, the net macroscopic current I flowing into the lamina is calculated by summing up the electric reactions corresponding to the boundary particles at which the negative electric potential is applied. Hence, using the

[3] The value of K_{e_1} calculated for MAT 2 is in perfect agreement with analytical calculations [57]

$$K_{e_1} = K_{\parallel} = K_{f\parallel} V_f + K_m (1 - V_f) \tag{83}$$

where $K_{\parallel}$ is the effective conductivity parallel to the direction of the fibers, whereas $K_{f\parallel}$ and K_m are the conductivity of the fibers and matrix, respectively.

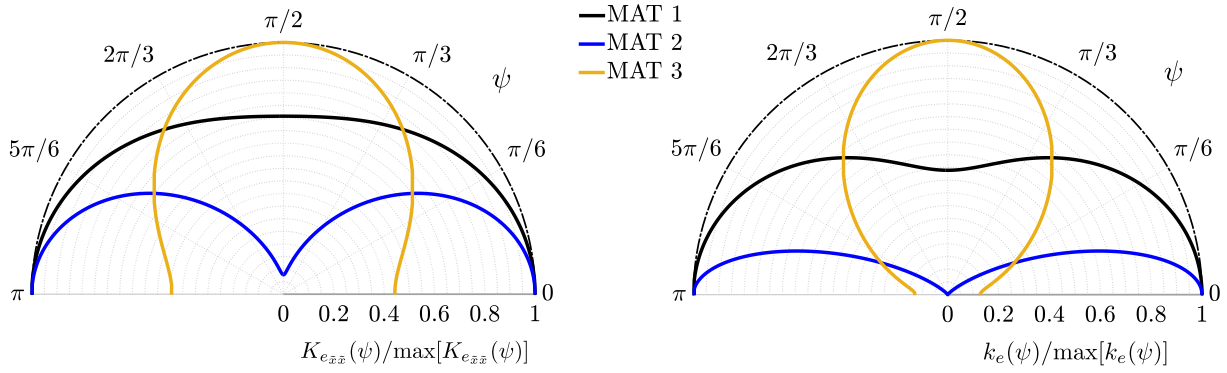

Figure 6: Homogenized conductive properties of the composite materials: Effective directional electrical conductivity corresponding to the three RVEs considered (left); Off-axis microelectrical conductivities as function of the ligament orientation angle ψ (right).

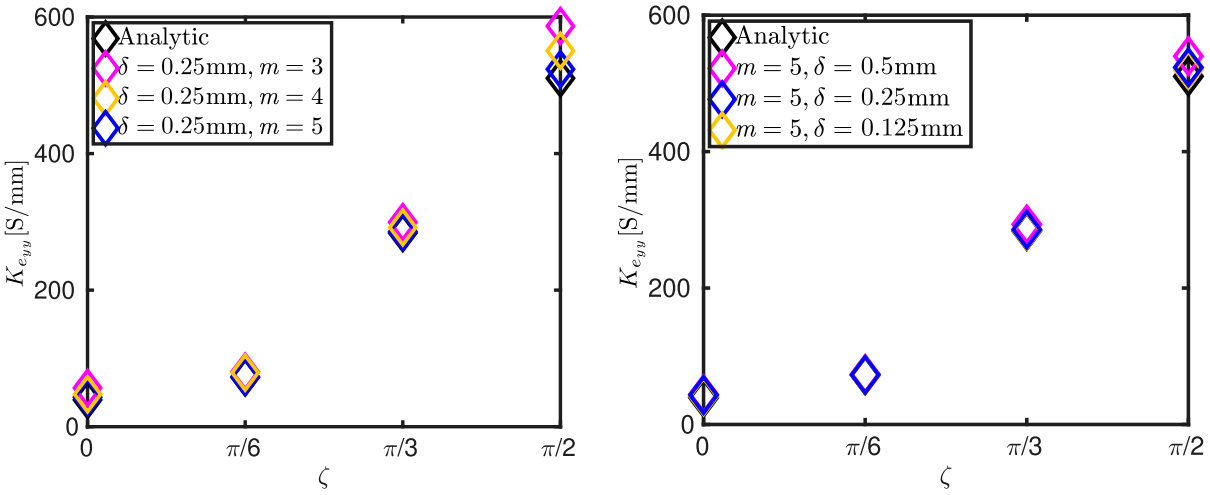

Figure 7: Analytic and computed effective off-axis conductivity $K_{e_{yy}}$ corresponding to different orientation of the material reference system ζ and adopting different discretization parameters of the proposed model.

equations

$$R(\zeta) = \Delta\phi / I(\zeta); \qquad K_{e_{yy}}(\zeta) = 2b / R(\zeta) hb \tag{84}$$

the electrical resistance R and the effective conductivity $K_{e_{yy}}$ are evaluated from the simulations for each angle of anisotropy ζ considered, and then compared to their theoretical values from Eq. 23. Results in Fig. 7 show that when $\pi/3 \geq \zeta \geq 0$, the model accurately predicts the material effective conductivity. For $\zeta = \pi/2$, however, even adopting a medium refined discretization, convergences to the theoretical result is obtained as the density parameter m increases. Adopting $m = 5$, the anisotropic conductive behavior can be accurately modeled. It is worth mentioning that for isotropic conductive materials, $m = 3$ has been proved to guarantee a good accuracy of the numerical solution [34], while for modelling anisotropic behavior using a discrete representation of bond properties in a two-parameters orthotropic non-local lattice, $m = 5$ was recommended [27, 30].

The effectiveness of the proposed formulation in predicting the electric field potential in anisotropic media is assessed by a square lamina with the geometry in 8, unitary thickness and made of material with the conductive properties of MAT 2 (2). The applied potential difference at the horizontal edge is $\Delta\phi = 20$ V, whereas the domain is discretized using a regular grid

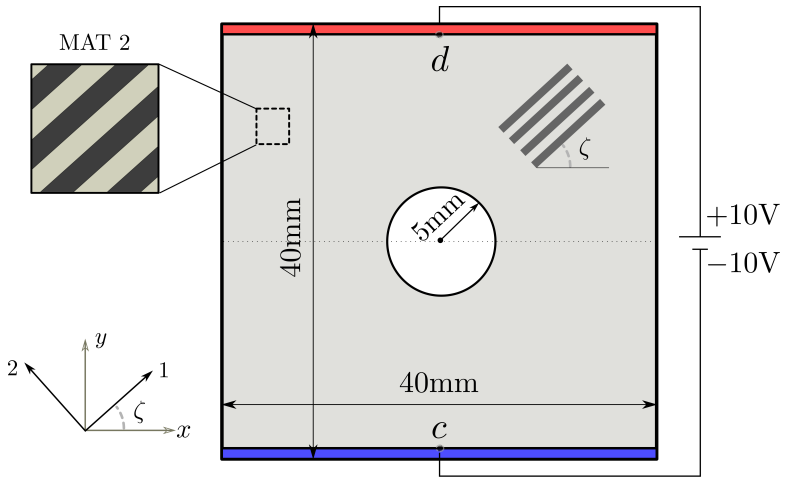

Figure 8: Square lamina with central hole and made of MAT 2: The electric potential is assigned at the top and bottom boundaries to produce a potential difference of $\Delta\phi$=20V.

spacing $\Delta x = 0.5$ mm resulting in a model of 6084 particles with $m = 5$ ($\delta = 2.5$ mm). The attention is here only on the electrical part of the model, hence no mechanical boundary conditions are considered in this section. The geometric features of the lamina are chosen to

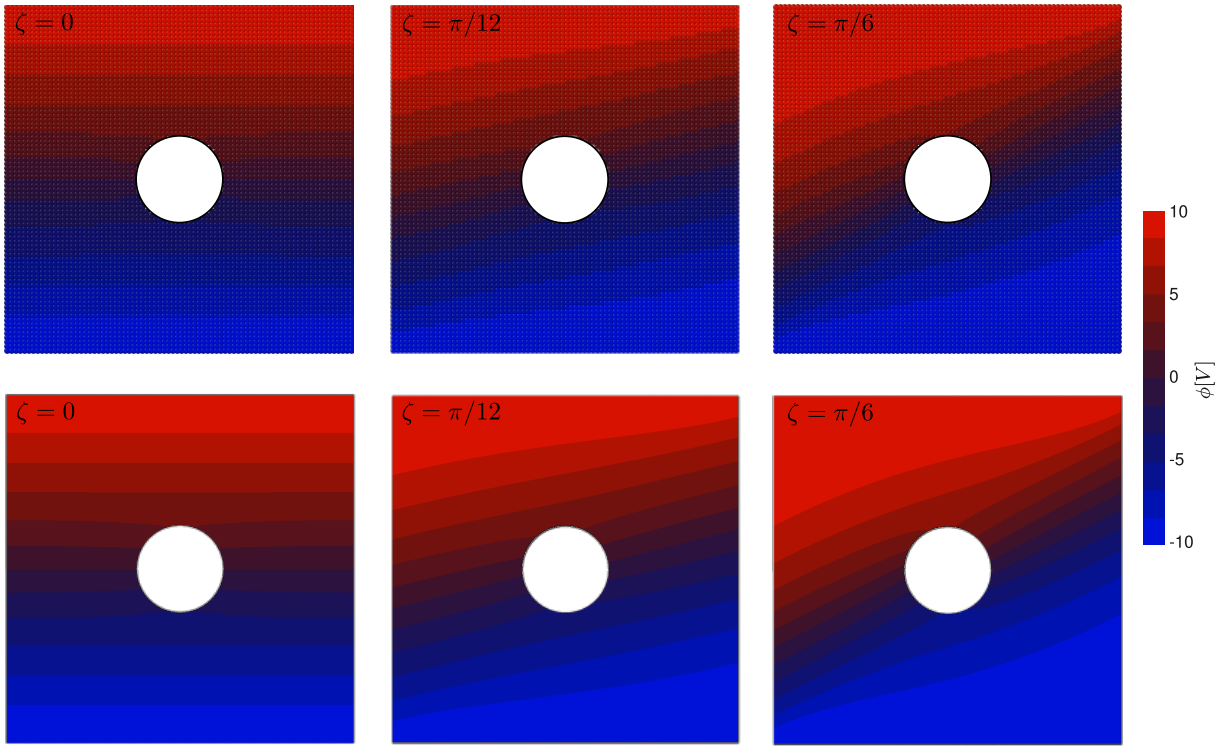

Figure 9: Square lamina with central hole and made of MAT 2: Solution obtained using the proposed model (top row) and FE (bottom row), and corresponding to angles of anisotropy $\zeta = 0$, $\zeta = \pi/12$ and $\zeta = \pi/6$.

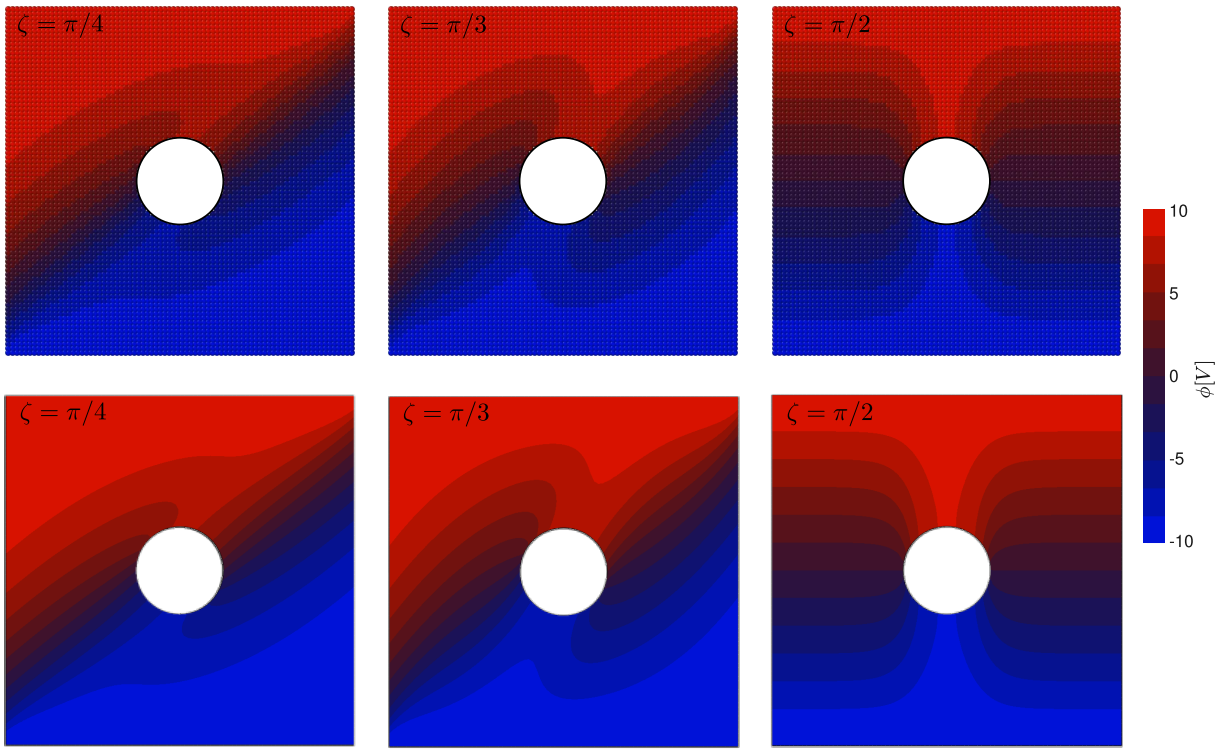

Figure 10: Square lamina with central hole and made of MAT 2: Solution obtained using the proposed model (top row) and FE (bottom row), and corresponding to angles of anisotropy $\zeta = \pi/4$, $\zeta = \pi/3$ and $\zeta = \pi/2$.

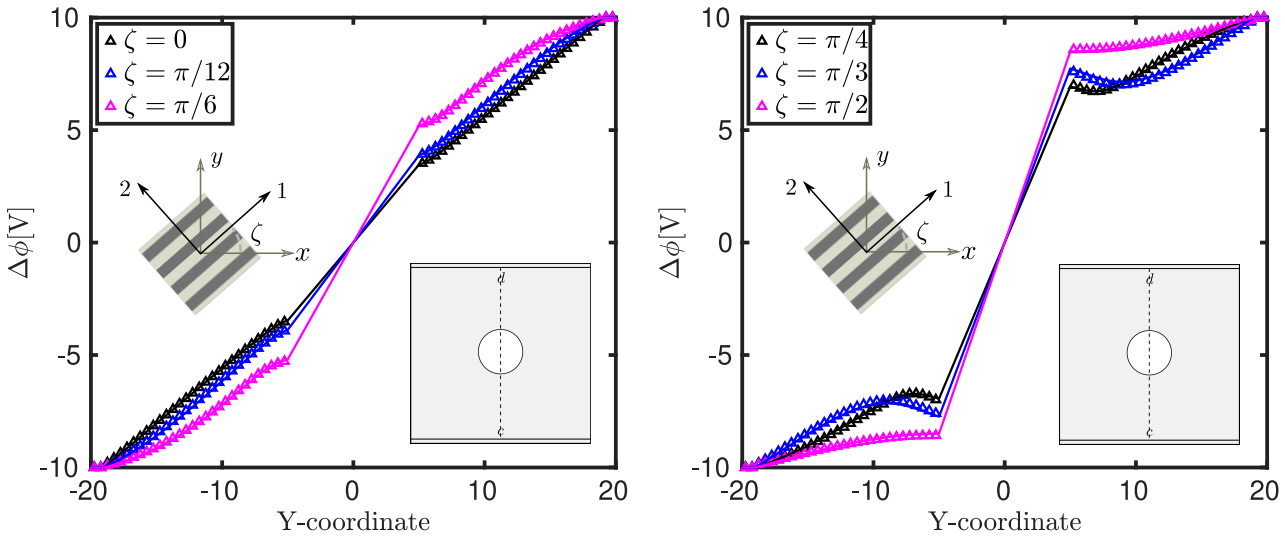

Figure 11: Square lamina with central hole and made of MAT 2: Comparison of nodal electric field potentials along the central vertical line connecting points d and c, between the FE (solid line) and proposed model (triangles) obtained with m=5 and $\Delta x = 0.25$ and considering different angles of anisotropy ζ.

obtain a non-homogeneous electric field, and the results obtained using the present formulation are compared to a FE model in which an irregular mesh of 6152 elements is adopted [4]. Figs. 9 and 10 show that predictions are in excellent agreement with the corresponding FEM solutions. A quantitative comparison of the electric potential along a central vertical line connecting points d and c (Fig. 8) is shown in Fig. 11. It confirms the accuracy of the proposed formulation and its numerical implementation.

[4]Four-nodes elements for coupled thermal-electrical analysis are used and uncoupled electrical analyses are performed by omitting the thermal properties from the material description. Hence only the electric potential degree of freedom is activated within the element and all heat transfer effects are ignored [34]

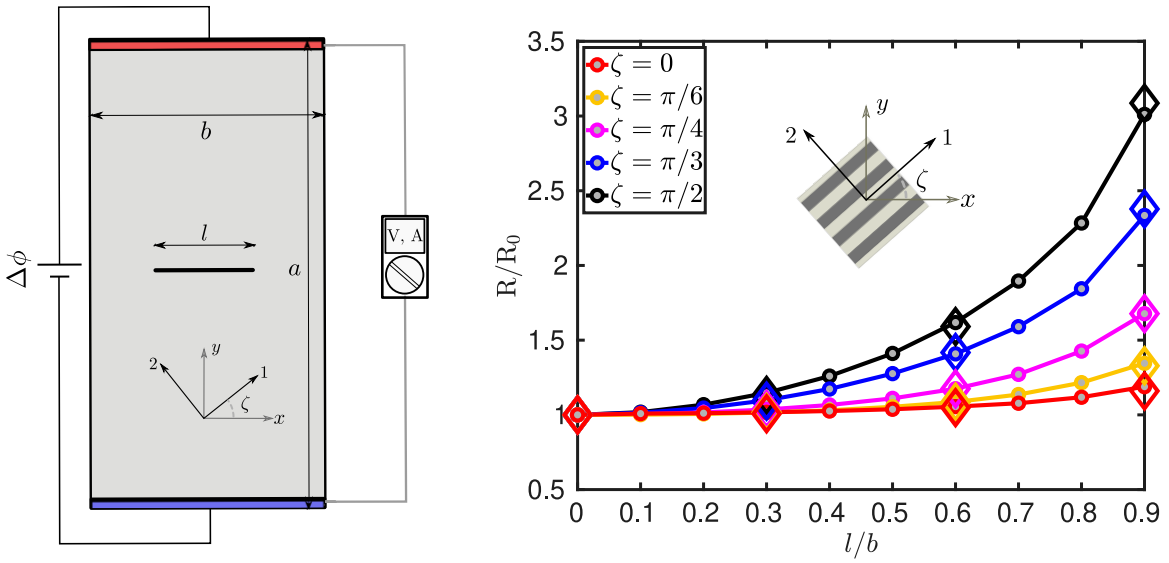

Figure 12: Electrical conduction in a orthotropic rectangular lamina made of MAT 2 with a horizontal crack: (left) Layout of the problem; (right) Variation of the electrical resistance as function of the propagating crack length for different ζ. The electrical resistances are normalized respect to the resistance R_0 corresponding to the uncracked lamina and the diamond markers represent finite element solutions.

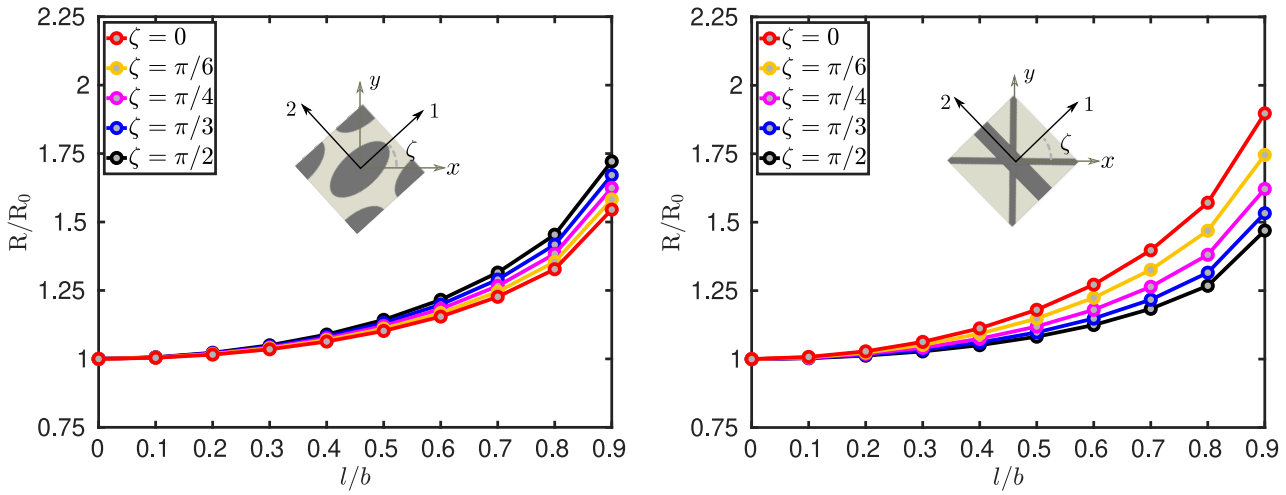

Figure 13: Variation of the electrical resistance in rectangular laminae made of MAT 1 (left) and MAT 3 (right) with a horizontal crack growth. The electrical resistances are normalized respect to the resistance R_0 corresponding to the uncracked laminae.

As third application, a preliminary assessment of the numerical performance of the proposed formulation is detailed for an orthotropic material with strong discontinuities such as cracks. The layout is shown in Fig. 12, where a=400mm and b =200mm, and the assigned length of the crack l is progressively increased from 0 to 0.9 b. The lamina is of unit thickness, effective anisotropic electrical conductive properties are those of the three materials considered, and an external electrical potential difference $\Delta\phi$=2V applied to the horizontal edges. The discretized model is composed by 3200 particles (regular grid of 80×40 particles with Δx = 5mm and $m = 5$). For each assigned pre-existing crack length, the electrical field potential is computed using the proposed model, then the net current I flowing into the lamina is estimated by the electrical reactions. In this way, applying Ohm's law the electrical resistance R is obtained for each crack length and for each orientation of the material reference system ζ. Results of numerical analyses are shown in Figs. 12 and 13. In Fig. 12, predictions of the present model for MAT 2 (the material characterized by the highest anisotropy) are compared to finite element results, again for highlighting the accuracy of the proposed anisotropic electrical model.

4.2. Fracture and damage sensing in conductive materials

The proposed anisotropic electromechanical formulation is adopted to model fracture and electrical conduction for damage sensing applications in cortical bone.

Bone is a conductive complex hierarchical composite which has natural mechanisms to resist fracture [58]. Actually, the simultaneous activation of toughening mechanisms by collagen fibers, lamellar structure of collagen fibers and osteon (Haversian canals) at various length scales provides enduring strength and toughness.

In particular, the results from the experimental campaign performed by Behiri and Bonfield [59, 60] are here considered to exploit the orientation dependence of the fracture of bovine cortical bone tissues. These authors employed the compact tension (CT) test to obtain stable crack propagation in fluid-saturated specimens at different orientations of the material reference system, so that the crack length and the corresponding load can be recorded during quasi-static loading [59]. Being cortical bone, in general, stronger in the longitudinal direction, loading conditions typical of CT test lead to final crack paths almost parallel to the osteons.

Failure properties of this specific material, homogenized as orthotropic medium, have been considered in other studies for the validation of orthotropic mechanical fracture models, as in the pioneering study by Ghajari et al [27]. However, it is worth underlying that differently from

other previous studies of cortical bone fracture using mechanical formulation based on elastic pair potentials as bond-based type formulations [29, 27], the here proposed model does not have any restriction in the number of material constants that define the effective in-plane orthotropy of the real material considered which is distinctively characterized by four independent elastic moduli. This result is obtained eliminating the central-force assumption for pairwise interactions. For bovine cortical bone, the elastic moduli were obtained from an experimental study by Van-Buskirk et al. [61, 27]. Assuming axis-1 to be parallel to the anatomical axis of the bone and 2-3 the plane of isotropy, C_{11}=25 GPa and C_{22}=16.25 GPa, whereas C_{12}=5.89 GPa and C_{66}=6.65 GPa.
Regarding failure properties, Behiri and Bonfield measured average critical stress intensity factors in transversely oriented bovine cortical bone ($\zeta = 0$ in Fig. 14), ranging from $K_{Ic2} = 3.2$ to 4.0 MPa.m$^{1/2}$ [62, 59, 60], whereas by grooving cortical bone compact tension specimens, they determined average values of K_{Ic1} from 6.3 to 6.5 MPa.m$^{1/2}$. It should be noted that no direct measures of the fracture energy of the longitudinal oriented material was performed by the authors in their experimental studies.
However, in order to define critical micropotential energy parameters of the proposed fracture model, critical strain energy release rates $G_{\zeta=0}$ and $G_{\zeta=\pi/2}$ are required. They were calculated, consistently with elastic moduli adopted for cortical bone, by energy-release rate proposed in [63] for a collinear extension of a pre-existing crack on one plane of material symmetry of an orthotropic material subjected to the loading conditions here considered

$$G_{\zeta=0} = \frac{1}{2} S_{22} \mathrm{Im}[-K_{Ic1}^2 (\mu_1 + \mu_2) \overline{\mu}_1 \overline{\mu}_2]; \quad G_{\zeta=\pi/2} = \frac{1}{2} S_{11} \mathrm{Im}[-K_{Ic2}^2 (\mu_1 + \mu_2) \overline{\mu}_1 \overline{\mu}_2] \tag{85}$$

where S_{ii} are components of the conventional compliance matrix (i.e. the inverse of matrix $\mathbf{C}$ in Eq. 50) and $\mu_1, \overline{\mu}_1$ or $\mu_2, \overline{\mu}_2$ are the conjugate pairs root of the characteristic equation [64] written as

$$S_{11}\mu^4 + (2S_{12} + S_{66})\,\mu^2 + S_{22} = 0; \qquad S_{22}\mu^4 + (2S_{12} + S_{66})\,\mu^2 + S_{11} = 0 \tag{86}$$

for $G_{\zeta=0}$ and $G_{\zeta=\pi/2}$, respectively.
The electrical conductivity of cortical bone tissues instead, were measured by Reddy and Saha

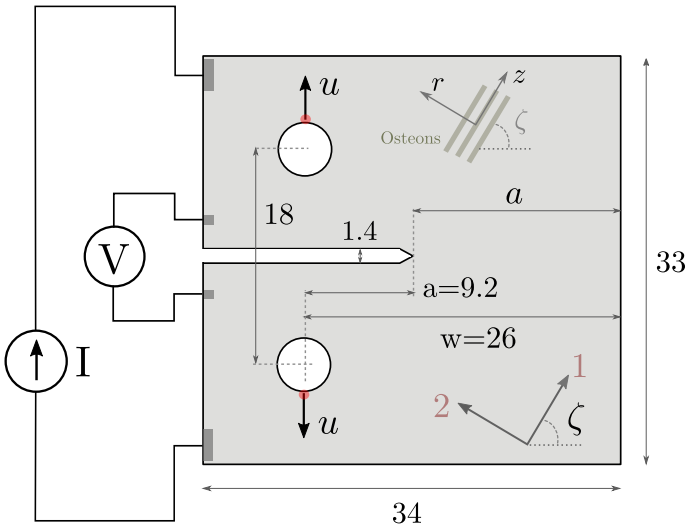

Figure 14: Layout of the compact tension test on cortical bone specimens at different angle of anisotropy ζ, and arrangement of current input leads and potential probe leads for potential drop crack length determination (dimensions in mm).

[65] in three orthogonal directions parallel to the principal directions of a long bone, demonstrating the anisotropic nature of this material. The electrical properties were found to be highly dependent on moisture content of bone and on frequency of the signal applied to the test specimen, being however nearly independent of frequency below 10 kHz [65]. In the case of wet (fluid-saturated) compact bovine bone at low-frequency or even DC conditions, the effective resistivity in the radial direction is approximately three times that in the longitudinal direction [65], which is consistent with the findings of Chakkalakal et al. [66]. In particular, resistivity in the radial direction is ρ_r=54 kΩcm, whereas in longitudinal direction ρ_z=17 kΩcm, hence $\rho_z/\rho_r \approx 3.2$. This anisotropic behavior of the electrical characteristics of bone is expected having higher porosity in the longitudinal direction due to the presence of Haversian canals [65].
The electromechanical setup under consideration is detailed in Fig. 14, where the longitudinal and radial axes are aligned with axes 1 and 2, respectively. Compact tension tests on cortical bone specimens in displacement control at different angle of anisotropy ζ as performed by Behiri and Bonfield [60] have been simulated using the proposed formulation. The mechanical and electrical conduction models have been then coupled, in the hypothesis of small deformations, [34] to study the effect of evolving discontinuities in cortical bone tissues effective conductive behavior using the potential drop crack length determination technique [67, 68]. In Fig. 14 both the loading zones and the arrangement of direct electrical current input leads and potential probe output leads are shown.
The microelastic moduli of the proposed mechanical model were calculated using Eqs. 64 and 65, while the micromoduli functions for cortical bone tissues were defined using Eqs. 55 and

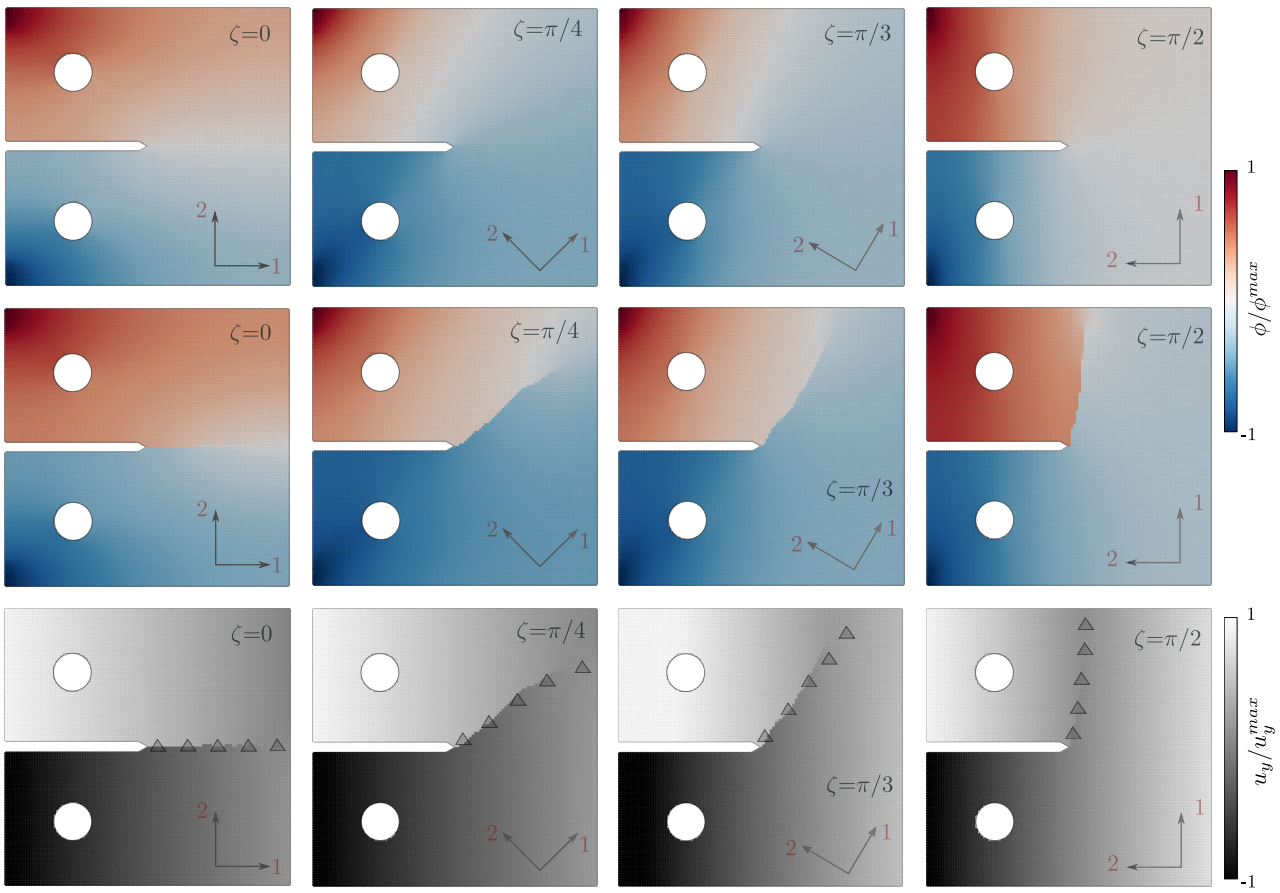

Figure 15: Fracture profiles and electric field potential in cortical bone specimens. First row: electric field potential of uncracked specimens. Second row: electric field potential of cracked specimens; Third row: displacement map of cracked specimens with indication of the experimental crack profiles from [60].

56. By considering the peculiarities of this material, critical micropotential energy function was determined using Eq. 70 along with Eq. 76, and adopting in Eqs. 85, the same values of the fracture toughness as in Ghajari et al. [27]. As for the electrical properties, the microconductivity function was determined using Eqs. 31-32.

The non-linear electromechanical problem was solved using different discretization parameters ($\delta = \delta_1$, $\delta = \delta_2$ and $m = 3.2$, $m = 5$) and displacement control with adaptive pseudo-time step refinement [69, 34]. It should be pointed out that our attention was focused on fracture and influence of crack propagation on effective macroscopic conductivity of the specimens at different ζ, hence other possible electromechanical interactions in cortical bone tissues have not been considered in this study. In any case, classic piezoelectric effects are observable only in dry bone tissues [70]. The results, obtained adopting an almost uniform grid spacing $\Delta x = 0.3$mm and $m = 5$, hence with $\delta = \delta_1 = 1.5$mm resulting in a model of 12312 particles, are shown in Fig. 15 along with experimental final crack path corresponding to angles of anisotropy $\zeta = 0$,

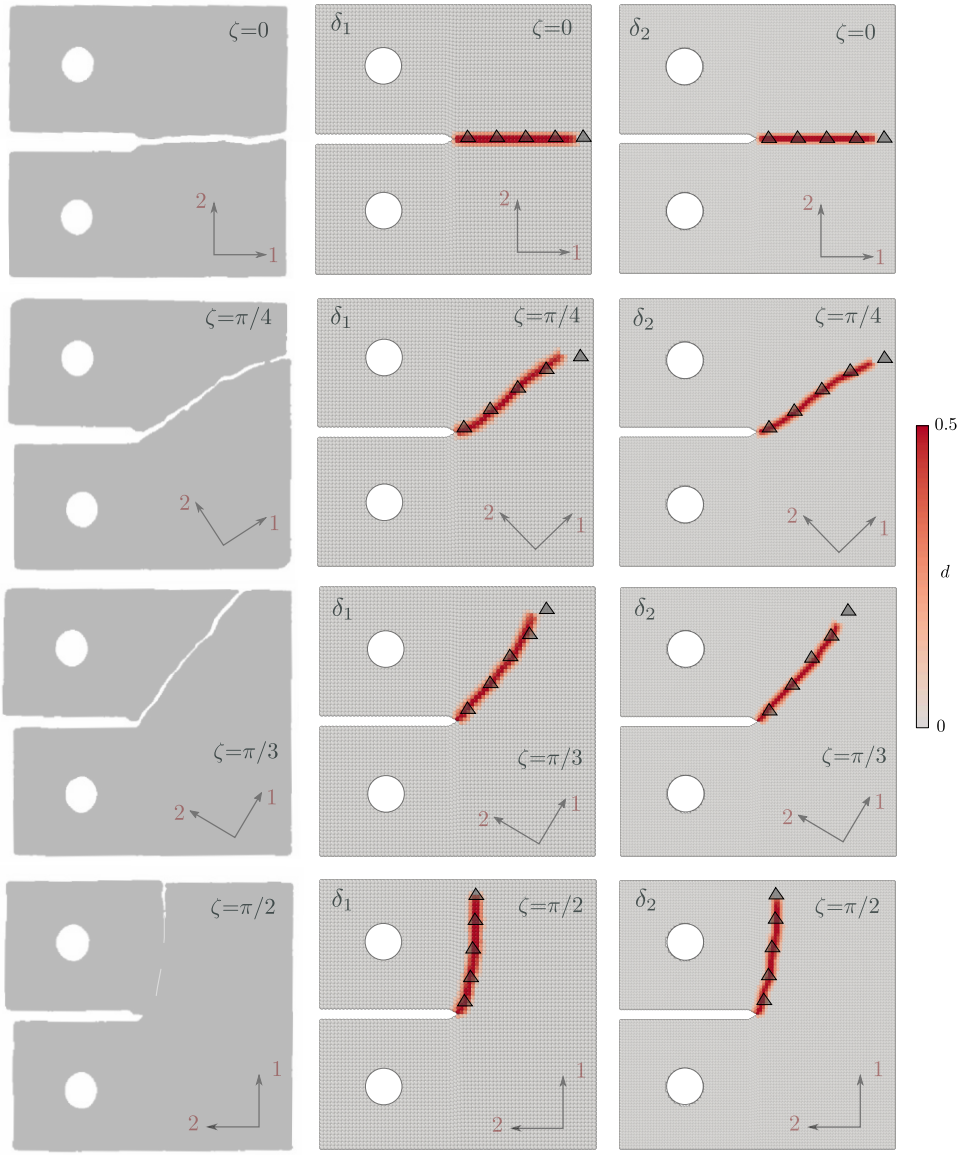

Figure 16: Fracture profiles of CT cortical bone specimens: Experimental [60] (left column and gray-filled triangles) and numerically predicted (central and right columns) crack propagation paths using $\delta = \delta_1$ and $\delta = \delta_2$ with $m = 3.2$ corresponding to angles of anisotropy ranging from $\zeta = 0$ to $\zeta = \pi/2$.

$\zeta = \pi/4$, $\zeta = \pi/3$ and $\zeta = \pi/2$. The crack paths predicted using the micropolar model and the proposed energetic failure criterion are in perfect agreement with experimental data [60]. It is interesting to note that experiments show quite complex fracture pattern, as can be seen from Figs. 15 and 16, especially for $\zeta = \pi/4$ and $\zeta = \pi/2$. Actually, the proposed model is able to predict the change of the average inclination angle of the fracture surface in cortical bone specimens inclined at $\pi/4$ and the initial deflection that the crack profile experiences when $\zeta = \pi/2$, before propagating straight along the "strongest" direction (see Fig. 15 and 16). Crack profiles agree very well with experiments (Fig. 16) even adopting coarser meshes and a lower value of the m parameter ($\Delta x = 0.47$mm with $m = 3.2$ [33], hence $\delta = \delta_1$ resulting in a model composed of 5472 particles, and $\Delta x = 0.35$mm with $m = 3.2$, hence $\delta = \delta_2 = 1.1$mm, resulting in a model composed of 8097 particles). It is consequence of the continuous functions used to model elasticity and fracture resistance of the material which allow the solution of this problem to be decoupled from the particles specific topology adopted. In any case it should be reminded that higher values of the exponent n in the anisotropic critical energy trigonometric function would require an higher value of the density parameter m, hence a finer angular discretization of Eq. 70.

Potential drop as function of the applied total displacement vs. force–displacement relationship corresponding to cortical bone specimens with material reference system inclined at $\zeta = 0$, $\zeta = \pi/4$, $\zeta = \pi/3$ and $\zeta = \pi/2$ are reported in 17. It is noted that the peak load corresponding to $\zeta = 0$ is $P = 96$ N. This value is in perfect agreement with the analytical value of $P = 98$ N determined on the basis of experimental data using the procedure reported in [59, 27] with

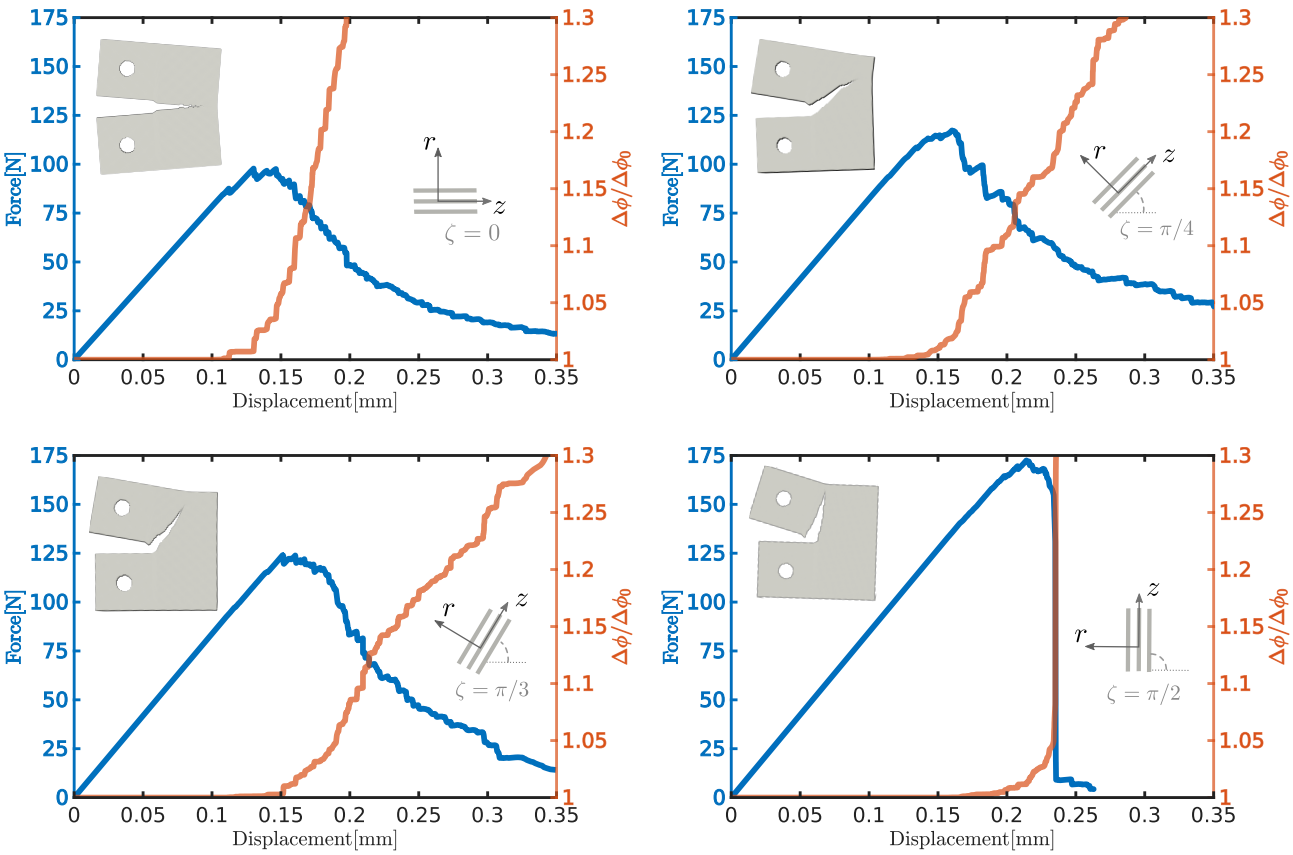

Figure 17: Potential drop and force-displacement relationship corresponding to cortical bone specimens with material reference system inclined at $\zeta = 0$, $\zeta = \pi/4$, $\zeta = \pi/3$ and $\zeta = \pi/2$. Results obtained using $\delta = \delta_1$ and $m = 5$.

$K_{Ic2} = 4.0\,\mathrm{MPa\,m^{1/2}}$ [62, 27] and thickness $h = 1$ mm.

It should be highlighted that in this study we adopted a two parameter function to describe the anisotropic resistance of cortical bone, however the proposed energetic criterion can be extended to other generalized multi-parameter directional dependent functions.

The average slope of the $\Delta\phi/\Delta\phi_0$ curves depend on the angle of anisotropy ζ, on the crack angle and crack pseudo-velocity. The latter effect can be excluded by reporting $\Delta\phi/\Delta\phi_0$ as function of the crack length measured during the simulation. In this way, each angle ζ was uniquely associated with a specific value of the average slope β of the $\Delta\phi/\Delta\phi_0$-l/a relationship, allowing for a direct determination of the actual crack length l from the value of $\Delta\phi$ registered by potential probe output leads (see Fig. 18). For the considered bone specimens, the angle β is proved to decrease non-linearly as function of the angle of anisotropy ζ, evidencing as expected, the sensitivity of the electric potential output probes which significantly decreases as the angle of anisotropy of the specimen approaches $\zeta = \pi/2$.

5. Conclusions

In this paper a continuum model was proposed based on pairwise interactions for electrical conduction, elasticity and fracture in conductive anisotropic materials. Using non-central elastic pair potentials and inelastic potential functions, the analytical formulation of a coupled electromechanical micropolar model was detailed characterized by six independent material moduli that define the in-plane behavior of orthotropic conductive materials. Elastic and conductive anisotropy of the material along with its non-uniform fracture resistance were modeled adopting continuous functions of the ligament orientation angle, allowing the mathematical formulation of the model to be, in principle, independent from the particles topology considered. Moreover, the elastic and conductive parameters of the model were derived using a generalized approach based on energetic equivalence, without the need for any particular assumption about the deformation and electric fields.

The accuracy of the proposed electromechanical model has been assessed by several examples that demonstrated its particular suitability in electromechanical problems involving discontinuities and fracture, such as the fracture and crack length determination by potential drop technique in anisotropic tissues. Further studies and experimental data are needed to extend the present formulation to other coupled phenomena.

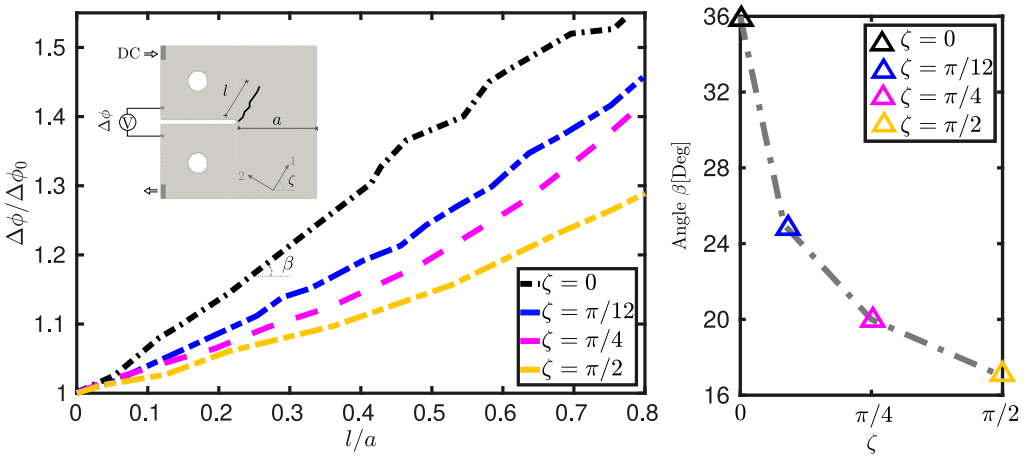

Figure 18: $\Delta\phi/\Delta\phi_0$ vs. normalized crack length l/a for direct determination of the actual crack length l from the value of $\Delta\phi$ registered by potential probe output leads (left); β as function of the angle of anisotropy ζ (right).

References

[1] Bobaru, F., Foster, J., Geubelle, P., Silling, S.. Handbook of peridynamic modeling. Advances in Applied Mathematics, CRC Press 2015;.

[2] Ostoja-Starzewski, M.. Lattice models in micromechanics. Applied Mechanics Reviews 2002;55(1):35–59.

[3] Casolo, S.. A linear-elastic heuristic-molecular modelling for plane isotropic micropolar and auxetic materials. International Journal of Solids and Structures 2021;224:111042.

[4] Gerstle, W.. Introduction to practical peridynamics: computational solid mechanics without stress and strain. World Scientific Publishing Co. Pte. Ltd.; 2016.

[5] Diana, V., Casolo, S.. A bond-based micropolar peridynamic model with shear deformability: Elasticity, failure properties and initial yield domains. International Journal of Solids and Structures 2019;160:201 – 231.

[6] Silling, S.. Reformulation of elasticity theory for discontinuities and long-range forces. Journal of the Mechanics and Physics of Solids 2000;48(1):175–209.

[7] Zhang, K., Ni, T., Sarego, G., Zaccariotto, M., Zhu, Q., Galvanetto, U.. Experimental and numerical fracture analysis of the plain and polyvinyl alcohol fiber-reinforced ultra-high-performance concrete structures. Theoretical and Applied Fracture Mechanics 2020;108:102566.

[8] Capecchi, D., Ruta, G.. The Theory of Elasticity in the 19th Century; vol. 52. Springer Verlag; 2015.

[9] Love, A.. A treatise on the Mathematical Theory of Elasticity. Dover, New York; 1944.

[10] Trageser, J., Seleson, P.. Peridynamics: a tale of two poissons ratios. Journal of Peridynamics and Nonlocal Modeling 2020;2:278 – 288.

[11] Silling, S., Epton, M., Weckner, O., Xu, J., Askari, E.. Peridynamic states and constitutive modeling. Journal of Elasticity 2007;88(2):151–184.

[12] Warren, T.L., Silling, S.A., Askari, A., Weckner, O., Epton, M.A., Xu, J.. A non-ordinary state-based peridynamic method to model solid material deformation and fracture. International Journal of Solids and Structures 2009;46(5):1186 – 1195.

[13] Tong, Y., Shen, W.Q., Shao, J.F.. An adaptive coupling method of state-based peridynamics theory and finite element method for modeling progressive failure process in cohesive materials. Computer Methods in Applied Mechanics and Engineering 2020;370:113248.

[14] Gerstle, W., Sau, N., Silling, S.. Peridynamic modeling of concrete structures. Nuclear Engineering and Design 2007;237(12):1250 – 1258.

[15] Zhang, Y., Pan, G., Zhang, Y., Haeri, S.. A multi-physics peridynamics-dem-ib-clbm framework for the prediction of erosive impact of solid particles in viscous fluids. Computer Methods in Applied Mechanics and Engineering 2019;352:675 – 690.

[16] Gerstle, W., Silling, S., Read, D., Tewary, V., Lehoucq, R.. Peridynamic simulation of electromigration. Tech Science Press 2008;8(2):75–92.

[17] Prakash, N., Seidel, G.D.. Effects of microscale damage evolution on piezoresistive sensing in nanocomposite bonded explosives under dynamic loading via electromechanical peridynamics. Modelling and Simulation in Materials Science and Engineering 2017;26(1):015003.

[18] Prakash, N., Seidel, G.D.. Electromechanical peridynamics modeling of piezoresistive response of carbon nanotube nanocomposites. Computational Materials Science 2016;113:154 – 170.

[19] Bobaru, F., Duangpanya, M.. The peridynamic formulation for transient heat conduction. International Journal of Heat and Mass Transfer 2010;53(19):4047 – 4059.

[20] Oterkus, S., Madenci, E., Agwai, A.. Peridynamic thermal diffusion. Journal of Computational Physics 2014;265:71 – 96.

[21] Chen, Z., Bobaru, F.. Peridynamic modeling of pitting corrosion damage. Journal of the Mechanics and Physics of Solids 2015;78:352 – 381.

[22] Bazazzadeh, S., Mossaiby, F., Shojaei, A.. An adaptive thermo-mechanical peridynamic model for fracture analysis in ceramics. Engineering Fracture Mechanics 2020;223:106708.

[23] Oterkus, S., Fox, J., Madenci, E.. Simulation of electro-migration through peridynamics. In: 2013 IEEE 63rd Electronic Components and Technology Conference. 2013, p. 1488–1493.

[24] Ni, T., Pesavento, F., Zaccariotto, M., Galvanetto, U., Zhu, Q.Z., Schrefler, B.A.. Hybrid fem and peridynamic simulation of hydraulic fracture propagation in saturated porous media. Computer Methods in Applied Mechanics and Engineering 2020;366:113101.

[25] Hattori, G., Trevelyan, J., Coombs, W.M.. A non-ordinary state-based peridynamics framework for anisotropic materials. Computer Methods in Applied Mechanics and Engineering 2018;339:416 – 442.

[26] Mikata, Y.. Linear peridynamics for isotropic and anisotropic materials. International Journal of Solids and Structures 2018;.

[27] Ghajari, M., Iannucci, L., Curtis, P.. A peridynamic material model for the analysis of dynamic crack propagation in orthotropic media. Computer Methods in Applied Mechanics and Engineering 2014;276:431 – 452.

[28] Zhang, H., Qiao, P.. A state-based peridynamic model for quantitative elastic and fracture analysis of orthotropic materials. Engineering Fracture Mechanics 2019;206:147 – 171.

[29] Ren, B., Wu, C., Seleson, P., Zeng, D., Lyu, D.. A peridynamic failure analysis of fiber-reinforced composite laminates using finite element discontinuous galerkin approximations. International Journal of Fracture 2018;214:49–68.

[30] Hu, W., Ha, Y.D., Bobaru, F.. Peridynamic model for dynamic fracture in unidirectional fiber-reinforced composites. Computer Methods in Applied Mechanics and Engineering 2012;217-220:247 – 261.

[31] Tian, D.L., Zhou, X.P.. A continuum-kinematics-inspired peridynamic model of anisotropic continua: Elasticity, damage, and fracture. International Journal of Mechanical Sciences 2021;199:106413.

[32] Voigt, W.. Lehrbuch der Kristallphysik 1928;.

[33] Diana, V., Ballarini, R.. Crack kinking in isotropic and orthotropic micropolar peridynamic solids. International Journal of Solids and Structures 2020;196-197:76–98.

[34] Diana, V., Carvelli, V.. An electromechanical micropolar peridynamic model. Computer Methods in Applied Mechanics and Engineering 2020;365:112998.

[35] Ostoja-Starzewski, M., Boccara, S.D., Jasiuk, I.. Couple-stress moduli and characteristics length of a two-phase composite. Mechanics Research Communications 1999;26(4):387 – 396.

[36] Bobaru, F.. Peridynamics and multiscale modeling. International Journal for Multiscale Computational Engineering 2011;9(6):vii–ix.

[37] Seleson, P.. Improved one-point quadrature algorithms for two-dimensional peridynamic models based on analytical calculations. Computer Methods in Applied Mechanics and Engineering 2014;282:184–217.

[38] Liu, W., Hong, J.W.. Discretized peridynamics for linear elastic solids. Computational Mechanics 2012;50(5):579–590.

[39] Le, Q.V., Bobaru, F.. Surface corrections for peridynamic models in elasticity and fracture. Computational Mechanics 2017;.

[40] Silling, S., Askari, E.. A meshfree method based on the peridynamic model of solid mechanics. Computers and Structures 2005;83(17-18):1526–1535.

[41] Diana, V., Casolo, S.. A full orthotropic micropolar peridynamic formulation for linearly elastic solids. International Journal of Mechanical Sciences 2019;160:140 – 155.

[42] Foster, J., Silling, S., Chen, W.. An energy based failure criterion for use with peridynamic states. International Journal for Multiscale Computational Engineering 2011;9(6):675–687.

[43] Panchadhara, R., Gordon, P.A.. Application of peridynamic stress intensity factors to dynamic fracture initiation and propagation. International Journal of Fracture 2016;201(1):81–96.

[44] Dipasquale, D., Zaccariotto, M., Galvanetto, U.. Crack propagation with adaptive grid refinement in 2d peridynamics. International Journal of Fracture 2014;190(1):1–22.

[45] Jiang, C., Zhao, G.F., Khalili, N.. On crack propagation in brittle material using the distinct lattice spring model. International Journal of Solids and Structures 2017;118-119:41 – 57.

[46] Wang, Y., Zhou, X., Wang, Y., Shou, Y.. A 3-d conjugated bond-pair-based peridynamic formulation for initiation and propagation of cracks in brittle solids. International Journal of Solids and Structures 2018;134:89 – 115.

[47] Zheng, G., Shen, G., Xia, Y., Hu, P.. A bond-based peridynamic model considering effects of particle rotation and shear influence coefficient. International Journal for Numerical Methods in Engineering 2020;121(1):93–109.

[48] Yu, H., Chen, X., Sun, Y.. A generalized bond-based peridynamic model for quasi-brittle materials enriched with bond tensionrotationshear coupling effects. Computer Methods in Applied Mechanics and Engineering 2020;372:113405.

[49] Prakash, N., Seidel, G.D.. Computational electromechanical peridynamics modeling of strain and damage sensing in nanocomposite bonded explosive materials (ncbx). Engineering Fracture Mechanics 2017;177:180 – 202.

[50] Mandal, T.K., Nguyen, V.P., Wu, J.Y.. A length scale insensitive anisotropic phase field fracture model for hyperelastic composites. International Journal of Mechanical Sciences 2020;188:105941.

[51] Li, B., Maurini, C.. Crack kinking in a variational phase-field model of brittle fracture with strongly anisotropic surface energy. Journal of the Mechanics and Physics of Solids 2019;125:502 – 522.

[52] Huang, Y., Ellingford, C., Bowen, C., McNally, T., Wu, D., Wan, C.. Tailoring the electrical and thermal conductivity of multi-component and multi-phase polymer composites. International Materials Reviews 2020;65(3):129–163.

[53] Koo, J.H.. Polymer nanocmposites: Processing, characterization, and applications. McGraw-Hill Nanoscience And Technology Series 2006;.

[54] Kushch, V.I.. Multipole Expansion Method in Micromechanics of Composites. Dordrecht: Springer Netherlands; 2013, p. 97–197.

[55] Yu, H., Heider, D., Advani, S.. Comparison of two finite element homogenization prediction approaches for through thickness thermal conductivity of particle embedded textile composites. Composite Structures 2015;133:719 – 726.

[56] Xiao, P., Yifeng, Z., Peng, W., Dan, L.. Estimation of thermal conduction in hollow-glass-beads-filled cement-based composites by variational asymptotic homogenization method. Applied Thermal Engineering 2019;161:114191.

[57] Liu, K., Takagi, H., Osugi, R., Yang, Z.. Effect of physicochemical structure of natural fiber on transverse thermal conductivity of unidirectional abaca/bamboo fiber composites. Composites Part A: Applied Science and Manufacturing 2012;43(8):1234 – 1241.

[58] Koester K., A.J., Ritchie, R.. The true toughness of human cortical bone measured with realistically short cracks. Nature Materials 2008;7:672–677.

[59] Behiri, J., Bonfield, W.. Orientation dependence of the fracture mechanics of cortical bone. Journal of Biomechanics 1989;22(8):863–872.

[60] Bonfield, W., Behiri, J.. Fracture toughness of natural composites with reference to cortical bone. Composite Materials Series 1989;6(C):615–635.

[61] Van-Buskirk, W., Owin, S., Ward, R.. Ultrasonic measurement of orthotropic elastic constants of bovine femoral bone. Journal of Biomechanicsl Engineering 1981;103:67–72.

[62] Behiri, J., Bonfield, W.. Fracture mechanics of bone-the effects of density, specimen thickness and crack velocity on longitudinal fracture. Journal of Biomechanics 1984;17(1):25–34.

[63] Azhdari, A., Nemat-Nasser, S.. Energy-release rate and crack kinking in anisotropic brittle solids. Journal of the Mechanics and Physics of Solids 1996;44(6):929–951.

[64] Lekhnitskii, S.G.. Theory of elasticity of an anisotropic body. San Francisco, CA: Holden-Day, Inc 1963;.

[65] Reddy, G.N., Saha, S.. Electrical and dielectric properties of wet bone as a function of frequency. IEEE Transactions on Biomedical Engineering 1984;BME-31(3):296–303.

[66] Chakkalakal, D.A., Johnson, M.W., Harper, R.A., Katz, J.L.. Dielectric properties of fluid-saturated bone. IEEE Transactions on Biomedical Engineering 1980;BME-27(2):95–100.

[67] Tong, J.. Notes on direct current potential drop calibration for crack growth in compact tension specimens. Journal of Testing and Evaluation 2001;29(4):402–406.

[68] Tarnowski K., N.K.D.D., Davies, D.. A unified potential drop calibration function for common crack growth specimens. Experimental Mechanics 2018;58:1003–1013.

[69] Ni, T., Zaccariotto, M., Zhu, Q.Z., Galvanetto, U.. Static solution of crack propagation problems in peridynamics. Computer Methods in Applied Mechanics and Engineering 2019;346:126–151.

[70] Reinish, G., A, N.. Piezoelectric properties of bone as functions of moisture content. Nature 1975;253:626–627.